UNIVERSITY
OF TRENTO

DIPARTIMENTO DI INGEGNERIA E SCIENZA DELL'INFORMAZIONE

38123 Povo – Trento (Italy), Via Sommarive 14
http://www.disi.unitn.it

MULTIPLE SHAPES RECONSTRUCTION BY MEANS OF MULTI-REGIONLEVELSETS

M. Benedetti, D. Lesselier, M. Lambert, and A. Massa

January 2011

Technical Report # DISI-11-090

Multiple Shapes Reconstruction by means of Multi-region Level Sets

M. Benedetti,[1] *Student Member, IEEE,* D. Lesselier,[2] *Member, IEEE,* M. Lambert,[2] and A. Massa,[1] *Member, IEEE*

[1] *ELEDIA* Research Group

Department of Information Engineering and Computer Science

University of Trento, Via Sommarive 14, 38050 Trento - Italy

Tel. +39 0461 882057, Fax. +39 0461 882093

E-mail: *andrea.massa@ing.unitn.it*, *manuel.benedetti@dit.unitn.it*

[2] Laboratoire des Signaux et Systèmes

Département de Recherche en Électromagnétisme

CNRS-SUPELEC-UPS11, 3 rue Joliot-Curie, 91192 Gif-sur-Yvette CEDEX, France

E-mail: *lesselier@lss.supelec.fr*

Multiple Shapes Reconstruction by means of Multi-region Level Sets

M. Benedetti, D. Lesselier, M. Lambert, and A. Massa

Abstract

In the framework of inverse scattering techniques for microwave imaging, this paper proposes an approach based on the integration between a multi-scaling procedure and the level-set-based optimization in order to properly deal with the shape reconstruction of multiple and disconnected homogeneous scatterers. The effectiveness and robustness of the proposed approach is assessed against both synthetic and experimental data. A selected set of results concerned with complex shapes is presented and discussed.

Key Words **-** Microwave Imaging, Inverse Scattering, Level Set, Multiscale Reconstruction, Multiple Objects, Homogeneous Scatterers.

1 Introduction

Short-range remote sensing methods are aimed at detecting targets buried in an inaccessible host domain as in nondestructive evaluation and testing (NDE/NDT) of industrial artifacts [1], subsoil inspection [2], biomedical imaging (BI) [3], and through-wall imaging (TWI) [4]. In order to effectively image the investigation area, X-rays, ultrasonics, eddy currents, and microwaves have been used. Microwave imaging techniques seemed to be very effective because of the ability of electromagnetic fields at centimeter wavelengths to penetrate non-ideal conductors [5]. Moreover, they usually require low power levels and are quite inexpensive. Furthermore, microwave imaging techniques do not need a mechanical contact between object and source and, unlike ultrasonics, a couplant is not usually necessary. On the other hand, they are operator/patient friendly [6] while a great care should be exercised when using X-rays.

Among microwave imaging modalities, inverse scattering techniques have been employed to obtain quantitative reconstructions of the domain under test in both 2-D [7]-[15] and 3-D geometries [16]-[20]. Notwithstanding the promising results [16]-[22], further efforts are still necessary to allow a massive employment in real applications. As a matter of fact, the underlying mathematical model is usually characterized by several drawbacks, such as ill-posedness [23] and non-linearity [24], that limit their feasibility because of the reduced achievable spatial resolution and the non-negligible computational costs. To mitigate the ill-posedness, multi-view/multi-illumination systems are adopted to collect a sufficient amount of data. However, the information available from the scattering experiments is upper-bounded and the number of independent data results lower than the dimension of the solution space [25][26]. Therefore, suitable strategies aimed at effectively exploiting the scattering data must be employed to increase the accuracy of the reconstruction process.

A possible solution is the use of multi-resolution strategies. The idea is that of using an enhanced spatial resolution only in those regions of interest (RoIs) where the unknown scatterers are supposed to be located [27] and/or where discontinuities occur [28][29]. Recently, adaptive multi-step approaches have been implemented to iteratively increase the spatial resolution through a "zooming" procedure [30][31]. Such a technique also keeps, during the inversion procedure, a fixed low ratio between unknowns and data in order to minimize the occurrence of local minima [26].

On the other hand, it should be also noticed that the lack of information causing the ill-posedness can be also reduced by exploiting when/if available the *a-priori* knowledge on the scenario under test. In several applications, the electromagnetic properties of the unknown targets are known and the objects lie within a known host medium. Moreover, depending on the required degree of accuracy, more complex scenarios can be approximated by a set of homogeneous regions with different shapes and parameters [32]. Under such an hypothesis and by assuming a suitable description of the Green's operator [33], the imaging problem reduces to the reconstruction of the support of a set of homogeneous regions (i.e., a shape retrieval procedure). Parametric techniques aimed at describing the unknown object by means of a finite set of suitable descriptors [34][36] or more sophisticated approaches based on evolutionary-controlled spline curves [37]-[38], shape gradients [39][40], level-sets [43]-[48], or binary profile [49][50] have been proposed. On the other hand, the support of simply-connected scatterers [51] can be also determined by means of the so-called *qualitative* methods [51]-[53].

As regards the level set description, it allows one to model complex shapes or regions in a simpler way, unlike pixel-based or parametric-based strategies. Within such a framework, an innovative strategy based on the integration of the iterative multi-scaling approach (*IMSA*) [30] and the level-set (*LS*) representation [45][46] has been recently proposed [54] to fully exploit the available *a-priori* information (e.g., the homogeneity of the scatterer) and the information content from the scattering measurements. Such an approach (called *IMSA-LS* in the following) has been validated in various scenarios characterized by one or multiple scatterers with complex shapes. Despite the accuracy of the reconstruction results and the reduction of the computational burden with respect to the standard strategy [45], such an implementation still needs some improvements to better deal with multiple disconnected objects. As a matter of fact, the spatial accuracy in resolving disconnected objects can be enhanced by associating to each scatterer a different RoI and processing the whole investigation domain as a collection of domains with different discretizations instead of using, at each reconstruction step, a unique grid within the whole scenario under test.

This paper focuses on the qualitative retrieval of multiple scatterers by adding some innovative features to the single-region implementation [54]. More specifically, a customized mathematical formulation for dealing with multiple disconnected RoIs, but also keeping the reliability

and efficiency of the previous approach in retrieving single shapes, is presented to define an unsupervised multi-scaling multi-region inversion procedure (*IMSMRA-LS*).

The outline of the paper is as follows. Section 2 presents the mathematical formulation of the multi-region strategy. A selected set of numerical results from the reconstructions of simple as well as complex shapes is presented and discussed in Sect. 3. Finally, some conclusions are drawn (Sect. 4).

2 Mathematical Formulation

With reference to a 2-D scalar electromagnetic inverse scattering problem [55], let us consider a set of P homogeneous obstacles with supports $D^{(p)}$, $p = 1, ..., P$, located in an inaccessible investigation domain D_I and characterized by known relative permittivity ε and conductivity σ (Fig. 1). Such a scenario is probed by a set of V transverse magnetic (*TM*) plane waves whose electric field $\underline{\zeta}^v(\underline{r})$, $v = 1, ..., V$, $\underline{r} = (x, y)$, is directed along the $\hat{\underline{z}}$ coordinate and parallel to the axis of the cylindrical geometry. The scattered field, $\underline{\xi}^v(\underline{r}) = \xi^v(\underline{r})\hat{\underline{z}}$, is collected at M measurement points located in a region, called observation domain D_O, external to the investigation domain.

In order to model the scenario under test, let us define the contrast function $\tau(\underline{r})$

$$\tau(\underline{r}) = \begin{cases} \tau & \underline{r} \in D^{(p)},\ p = 1, ..., P \\ 0 & \text{otherwise} \end{cases} \tag{1}$$

where $\tau = (\varepsilon - 1) - j\frac{\sigma}{2\pi f \varepsilon_0}$, f and ε_0 being the working frequency and the background permittivity, respectively. As regards the scattering phenomena, the interactions between objects and fields are described by the following integral equations

$$\xi^v(\underline{r}_m) = \left(\frac{2\pi}{\lambda}\right)^2 \int_{D_I} \tau(\underline{r}')\, E^v(\underline{r}')\, G_{2D}(\underline{r}_m/\underline{r}')\, d\underline{r}', \quad \underline{r}_m \in D_O \tag{2}$$

$$E^v(\underline{r}) = \zeta^v(\underline{r}) + \left(\frac{2\pi}{\lambda}\right)^2 \int_{D_I} \tau(\underline{r}')\, E^v(\underline{r}')\, G_{2D}(\underline{r}/\underline{r}')\, d\underline{r}', \quad \underline{r} \in D_I \tag{3}$$

where λ is the background wavelength, E^v is the total electric field, and $G_{2D}(\underline{r}/\underline{r}') = -\frac{j}{4}H_0^{(2)}\left(\frac{2\pi}{\lambda}\|\underline{r} - \underline{r}'\|\right)$

is the free-space 2-D Green's function, $H_0^{(2)}$ being the second-kind 0-th order Hankel function. As far as the qualitative imaging of a single scatterer is concerned, the inverse scattering problem described by (2) and (3) has been solved in [54] by means of the *IMSA-LS*. The unknown shape and position of the target have been retrieved by nesting a *LS* reconstruction procedure into a multi-step process (s being the step index). More in detail, at each step of the *IMSA*, the iterative ($k^{(s)}$ being the iteration index) *LS* procedure minimizes the cost function Θ

$$\Theta\left\{\phi_k^{(s)}\right\} = \frac{\sum_{v=1}^{V}\sum_{m=1}^{M}\left|\Im_{m,v}\left\{\phi_k^{(s)}\right\} - \xi_{meas}^{v}\left(\underline{r}_m\right)\right|^2}{\sum_{v=1}^{V}\sum_{m=1}^{M}\left|\xi_{meas}^{v}\left(\underline{r}_m\right)\right|^2}, \tag{4}$$

which quantifies the discrepancy between the measured scattered field $\xi_{meas}^{v}\left(\underline{r}_m\right)$ and the reconstructed field $\Im_{m,v}\left\{\phi_k^{(s)}\right\}$ computed from the current estimate of the level set function, $\phi_k^{(s)}$. In order to properly take into account the presence of multiple disconnected scatterers, an enhancement and an extension of the *IMSA-LS* are necessary. Besides a suitable generalization of the $IMSA-LS$ architecture proposed in [54] to deal with single scatterers, the presence of multiple RoIs is addressed by defining the following new procedural operations iteratively repeated at each step s:

- *Multi-Region Level Set Representation*, aimed at defining a suitable representation of the problem unknown when considering $Q^{(s)}$ regions of interest, $R^{(q)}$, $q = 1, ..., Q^{(s)}$, $s = 1, ..., S$;
- *Termination Procedure*, aimed at stopping the LS-based iterative minimization performed at each step s;
- *RoI Detection*, aimed at determining the number $Q^{(s+1)}$ and the extension of the RoIs at the $(s+1)$-th step starting from the reconstructed shape at the previous one.

2.1 Multi-Region Level Set Representation

At each step s of the *IMSA* and according to the multi-region multi-resolution representation, a higher resolution level ($i = s$) is adopted to describe the level set function $\phi^{(s)}\left(\underline{r}\right)$ only inside the *RoI*s, $R^{(q)}$, $q = 1, ..., Q^{(s)}$, while the same spatial accuracy adopted at the $(s-1)$-th step is kept unaltered in the remaining part of D_I. More in detail, if $s = 1$, the unique ($Q^{(1)} = 1$)

region of interest $R^{(1)}$ extends to the whole investigation domain, $R^{(1)} \equiv D_I$, and the level set function is then expressed as the following N-elements (N being the number of discretization subdomains chosen according to the degrees-of-freedom of the scattered field [25][26]) linear combination

$$\phi^{(1)}\left(\underline{r}\right) = \sum_{n=1}^{N} \phi_n \mathcal{B}\left(\underline{r}_n\right) \tag{5}$$

where $\mathcal{B}\left(\underline{r}_n\right)$ is a rectangular basis function whose support is centered at the n-th partition subdomain of $R^{(1)}$, $R_n^{(1)}$. Otherwise ($s > 1$), each region of interest $R^{(q)}$, $q = 1, ..., Q^{(s)}$, is partitioned into $N^{(q)}$ sub-domains, $\sum_{q=1}^{Q^{(s)}} N^{(q)} = N$, and the multi-region multi-resolution representation of the level set function is adopted (Fig. 1)

$$\phi^{(s)}\left(\underline{r}\right) = \sum_{i=1}^{s} \sum_{q=1}^{Q^{(i)}} \sum_{n=1}^{N^{(q)}} \phi_n^{(q)} \mathcal{B}\left(\underline{r}_n^{(q)}\right) \tag{6}$$

where $\mathcal{B}\left(\underline{r}_n^{(q)}\right)$ is equal to 1 if $\underline{r}_n^{(q)} \in R_n^{(q)}$ and 0 otherwise. Moreover, $\phi_n^{(q)}$ indicates the constant value of the level set function within the sub-domain $R_n^{(q)}$ of the q-th region of interest ($q = 1, ..., Q^{(s)}$). As regards $N^{(q)}$, it is defined as

$$N^{(q)} = \left\lfloor N \frac{A^{(q)}}{\sum_{q=1}^{Q^{(s)}} A^{(q)}} \right\rfloor \tag{7}$$

to have the same spatial resolution in every *RoI*s, $\lfloor \cdot \rfloor$ being the floor function and $A^{(q)}$ is the area of $R^{(q)}$. According to the multi-region multi-resolution representation of the level set function, Equation (2) assumes the following form

$$\Im_{m,v}\left\{\phi^{(s)}\right\} = \sum_{i=1}^{s} \sum_{q=1}^{Q^{(i)}} \sum_{n=1}^{N^{(q)}} \tau \left[1 - H\left\{\phi^{(s)}\left(\underline{r}_n^{(q)}\right)\right\}\right] \mathcal{B}\left(\underline{r}_n^{(q)}\right) E^v\left(\underline{r}_n^{(q)}\right) G^{(i)}\left(\underline{r}_m / \underline{r}_n^{(q)}\right) \quad \underline{r}_m \in D_O \tag{8}$$

where $H\{\,.\,\}$ is the Heaviside step function equal to 0 if its argument is negative and 0 1 otherwise, and

$$G^{(i)}\left(\underline{r}/\underline{r}_n^{(q)}\right) = G_{2D}\left(\underline{r}/\underline{r}_n^{(q)}\right) A_n^{(q)}, \quad \underline{r}_n^{(q)} \in R_n^{(q)},\ q = 1, ..., Q^{(i)},\ i = 1, ..., S. \tag{9}$$

Moreover, the value of $E^v\left(\underline{r}_n^{(q)}\right)$ is numerically determined by solving (3) in its multi-scale form

$$E^v\left(\underline{r}_n^{(q)}\right)=\sum_{i=1}^{s}\sum_{q=1}^{Q^{(i)}}\sum_{n=1}^{N^{(q)}}\zeta^v\left(\underline{r}_p^{(q)}\right)\left[1-\tau\left[1-H\left\{\phi^{(s)}\left(\underline{r}_n^{(q)}\right)\right\}\right]G^{(i)}\left(\underline{r}_n^{(q)},\underline{r}_p^{(q)}\right)\right]^{-1},\quad \underline{r}_n^{(q)}\in D_I \tag{10}$$

with a standard direct solver.

2.2 Termination Criterion

At each step s, the LS-based inversion is stopped when either (*a*) the reconstruction is "stable" or (*b*) a maximum number of iterations is reached ($k=K$) or the value of the cost function (4) is smaller than a fixed threshold γ [i.e., $\Theta\left\{\phi_k^{(s)}\right\}<\gamma$, $k=k_{opt}$]. As far as the stability of the reconstruction is concerned, it is verified when the following conditions hold true:

- ***Shape Stability*** - Unlike the standard pixel-based criterion[(1)] used for quantitative imaging, a technique based on the Hausdorff distance $\mathcal{L}$ [56][57]-[59] is adopted to properly deal with shape reconstruction. It is based on the computation of the value of the Hausdorff distance between the contour of the $(k-h)$-th estimated shape in $R^{(q)}$, $\partial D_{k-h}^{(q)}$, and the current one, $\partial D_k^{(q)}$, for a fixed number of iterations, $h=1,...,K_{\mathcal{L}}$

$$\mathcal{L}_{kh}=\max\left\{\max_a\min_b\left[|\underline{r}_a-\underline{r}_b|\right],\max_b\min_a\left[|\underline{r}_a-\underline{r}_b|\right]\right\} \tag{11}$$

  where $\underline{r}_b$, $b=1,...,B_k^{(q)}$, and $\underline{r}_a$, $a=1,...,B_{k-h}^{(q)}$, are the centers of the sub-domains to which the contours $\partial D_k^{(q)}$ [i.e., $\phi_k^{(s)}\left(\underline{r}_b\right)=0$] and $\partial D_{k-h}^{(q)}$ [i.e., $\phi_{k-h}^{(s)}\left(\underline{r}_a\right)=0$] belong, respectively. Then, the stability takes place when

$$\max_{h=1,...,K_{\mathcal{L}}}\left\{\frac{\mathcal{L}_{hk}}{\ell^{(q)}}\right\}<\gamma_{\mathcal{L}} \tag{12}$$

  $\gamma_{\mathcal{L}}$ being a user-defined threshold and $\ell^{(q)}=\sqrt{2\frac{A^{(q)}}{N^{(q)}}}$ is the spatial resolution in each RoI, $R^{(q)}$, $q=1,...,Q^{(s)}$ [Fig. 2(*a*)];

(1) The standard pixel-based stability criterion based on the comparison between the pixels of the reconstructions at two different iterations [54] is not suitable for LS-based algorithms, since when a "blinking" behavior arises during the iterative process without significantly modifying the estimated shapes (i.e., a small amount of pixels of the reconstruction intermittently turns up), the stability condition does not hold true.

- ***Cost Function Stationariness*** - Likewise [54], the cost function is assumed to be stationary when its variations are numerically negligible within a window of K_Θ iterations. This is assessed by evaluating the variance of the values $\Theta\left\{\phi_h^{(s)}\right\}$, $h = 1, .., K_\Theta$.

If the convergence of the iterative process is successful, the process is stopped by setting $\phi^{(s)} = \phi_k^{(s)}$ and performing the RoIs detection. Otherwise, the iteration index is increased ($k \rightarrow k+1$) and the level set function is updated within the q-th RoI by solving the Hamilton-Jacobi equation

$$\phi_k^{(s)}\left(\underline{r}_n^{(q)}\right) = \phi_{k-1}^{(s)}\left(\underline{r}_n^{(q)}\right) - \Delta t_k^{(s)} v_{k-1}^{(s)}\left(\underline{r}_n^{(q)}\right) \Psi\left\{\phi_{k-1}^{(s)}\left(\underline{r}_n^{(q)}\right)\right\}, \quad \underline{r}_n^{(q)} \in R^{(q)},\ q = 1, ..., Q^{(s)} \tag{13}$$

where $\Psi\{\cdot\}$ is the numerical Hamiltonian and v indicates the velocity function [54]. Furthermore, Δt is the time-step chosen according to the Courant-Friedrich-Leroy condition [41][42] and defined as follows

$$\Delta t_k^{(s)} = \frac{\ell^{(q)}}{\max_{\underline{r}}\left\{v_k^{(s)}\left(\underline{r}\right)\right\}}. \tag{14}$$

2.3 RoIs Detection

Until the convergence [54] ($s = s_{opt}$), the RoIs at the $(s+1)$-th step are defined as the rectangular regions $R^{(q)}$, $q = 1, ..., Q^{(s+1)}$, containing the contours $\partial D^{(q)}$, $q = 1, ..., Q^{(s+1)}$. In order to determine the locations and extensions of the RoIs, the definition of closed curves in [60] is exploited to overcome the limitations of other and well-known topology theories in dealing with practical purposes. More specifically, starting from the distribution of the level set function at the s-th step, $\phi^{(s)}\left(\underline{r}\right)$, an estimate of the q-th object contour, $\partial D^{(q)}$, $q = 1, ..., Q^{(s+1)}$, is given by determining the set of discretization domains whose locations $\underline{r}_b$, $b = 1, ..., B_k^{(q)}$, satisfy the following conditions [60]

$$\begin{gathered} \phi^{(s)}\left(\underline{r}_b\right) = 0 \\ 0 < |x_b - x_{b+1}| + |y_b - y_{b+1}| \leq 2\ell^{(q)} \end{gathered}. \tag{15}$$

When the coordinates $(x_b,\, y_b)$ of the $B_k^{(q)}$ subdomains belonging to the 8-connected simple closed curves [60] that edge the targets [Fig. 2(*b*)] are available, the RoIs are then identified by computing their centers, $\underline{r}^{(q)}$, $q = 1, ..., Q^{(s+1)}$,

$$x^{(q)} = \frac{\sum_{b=1}^{B^{(q)}} x_b}{B^{(q)}}, \quad y^{(q)} = \frac{\sum_{b=1}^{B^{(q)}} y_b}{B^{(q)}}, \tag{16}$$

and the corresponding sides, $L_x^{(q)}$, $L_y^{(q)}$, $q = 1, ..., Q^{(s+1)}$,

$$L_x^{(q)} = \max_{b,a \in \left[1,\, B^{(q)}\right]} \left[|x_b - x_a|\right], \quad L_y^{(q)} = \max_{b,a \in \left[1,\, B^{(q)}\right]} \left[|y_b - y_a|\right]. \tag{17}$$

3 Numerical Validation

To show the effectiveness and limitations of the proposed approach, this section discusses the results from a selected set of inversions concerned with different geometries including a set of experimental data collected in a controlled environment [61].

3.1 Analysis of the Robustness

The first test case is concerned with the reconstruction of three off-centered scatterers with complex shapes. The objects whose contours are indicated by the red dashed lines in Figs. 3(*a*)-3(*c*)-3(*e*) have known dielectric permittivity equal to $\varepsilon = 1.8$. Such a scenario has been illuminated from $V = 40$ directions, $\theta_v = 2\pi \frac{(v-1)}{V}$, $v = 1, ..., V$, and the scattered field has been collected at $M = 40$ (i.e., $M = V$ since each probe can act as electromagnetic source/receiver) equally-spaced angular locations on a circle $\rho = 5\lambda$ in radius external to the investigation domain $L = 5\ \lambda$-sided. The number of measurement points has been chosen to take into account the degrees of freedom of the scattered fields,which depends on the size of the investigation domain [25], and to collect all the information "coded" in the measured data.

As far as the initialization of the *IMSMRA-LS* technique is concerned, a centered circular scatterer of radius $\frac{\lambda}{2}$ and permittivity $\varepsilon_a = \varepsilon$ has been chosen as guess solution and the RoI has been partitioned into $N^{(1)} = 29 \times 29$ sub-domains according to the guidelines suggested in

[26] to minimize the occurrence of local minima. Moreover, the maximum number of RoIs has been set to $Q = 10$. Concerning the stopping criterion, the following thresholds have been adopted: $S = 5$ (maximum number of steps), $K = 500$ (maximum number of iterations), and $K_\Theta = K_\mathcal{L} = \frac{K}{10}$ (stability counters). The choice of the optimization threshold $\gamma_\mathcal{L}$ strongly influences the trade-off between reconstruction accuracy and convergence rate of the iterative process. More specifically, $\gamma_\mathcal{L} = 0$ forces the "Shape Stability" condition to hold true only when the current shape is equal to those estimated at the $(k-h)$-th, $h = 1, ..., K_\mathcal{L}$, previous iterations. On the contrary, a high value of $\gamma_\mathcal{L}$ may cause a premature convergence of the iterative process to a wrong solution. A good trade-off between convergence rate and reconstruction accuracy is generally obtained by setting $1 < \gamma_\mathcal{L} < 2$ (i.e., the Hausdorff distance between $\ell^{(q)}$ and $2\ell^{(q)}$). After a detailed heuristic analysis (not reported here for want of space), $\gamma_\mathcal{L}$ has been set to 1.5 throughout the numerical validation.

As a representative result, Figure 3 shows the reconstructed profile in correspondence with blurred data characterized by a signal-to-noise-ratio (SNR) value

$$SNR = 10log\left\{\frac{\sum_{v=1}^{V}\sum_{m=1}^{M}\left|\xi^v\left(\underline{r}_m\right)\right|^2}{\sum_{v=1}^{V}\sum_{m=1}^{M}\left|\mu^{v,m}\right|^2}\right\} \tag{18}$$

equal to $SNR = 20\,dB$, $\mu^{v,m}$ being a complex Gaussian random variable with zero mean value. At the first step [$s = 1$ - Fig. 3(*a*)], the supports of the scatterers are inaccurately estimated although their centers turn out to be close to the actual ones. Thanks to enhanced spatial resolution within the RoIs, the reconstruction accuracy improves at the successive step [$s = 2$ - Fig. 3(*c*)] as confirmed by the quantitative indexes in Tab. I, δ and Δ being the values of the localization error and the support estimation error [30][36], respectively. At the convergence ($s = s_{opt} = 3$), $Q^{(s)} = 3$ RoIs discretized into $N^{(1)} = 18 \times 18$, $N^{(2)} = 15 \times 15$, and $N^{(3)} = 16 \times 16$ cells are properly identified and the object shapes fairly retrieved. When reducing the number V of views, the amount of information is not enough to reach the same reconstruction accuracy. As a matter of fact, the average reconstruction errors, $< \delta >$ and $< \Delta >$, get sensibly worse as V decreases (e.g., $< \delta >_{V=30} = 4.2 \times 10^{-2}$, $< \Delta >_{V=30} = 4.9 \times 10^{-3}$; $< \delta >_{V=20} = 5.2 \times 10^{-2}$, $< \Delta >_{V=20} = 9.0 \times 10^{-3}$; $< \delta >_{V=10} = 8.7 \times 10^{-2}$, $< \Delta >_{V=10} = 1.93 \times 10^{-2}$).

For completeness, the plot of the multi-resolution level set $\phi^{(s)}$ at different steps is shown [$s = 1$

- Fig. 3(*b*), $s = 2$ - Fig. 3(*d*), and $s = s_{opt} = 3$ - Fig. 3(*f*)] and the behavior of the cost function $\Theta_k^{(s)}$ versus the iteration index k is reported in Fig. 4. It is worth to notice that the level set distribution within the investigation domain is quite different from the object function behavior and it determines, instead of the distribution of the object function itself, the evolution of the reconstruction during the iterative process. The final results and the corresponding level set functions for the *IMSA-LS* [54] [Figs. 5(*a*)-(*b*) - $N = 29 \times 29$] and the *Bare LS* [Fig. 5(*c*)-(*d*) - $N = 50 \times 50$] are also given for a comparative analysis. From the comparison, the reconstructions without the multi-region detection appear to be less accurate and the decrease of the misfit function worsen (Fig. 4). The single-region approach does not perform an accurate data inversion, although the scatterers are still well localized [Fig. 5(*a*)]. As a matter of fact, the actual objects are too far to allow a suitable allocation of the unknowns for achieving a satisfactory spatial resolution within the unique *RoI* and the multi-step process stops at $s = s_{opt} = 1$. On the other hand, the *Bare LS* is able to detect only two scatterers, while the third one is fully omitted. A summary of the results in terms of the quantitative error indexes is given in Tab. I.

As regards the data fitting, the plots of the misfit function in Fig. 4 show a similar behavior between the *IMSA-LS* and the multi-region strategy only at the initial step just during the first iterations, while the multi-region implementation guarantees a better fitting with the scattering data. As expected, a more significant mismatch is present in correspondence with the *Bare LS* inversion because of the failure of the approach in detecting the hollow cylinder.

Concerning the computational issues, since the complexity of the algorithm is of order $\mathcal{O}\left(2 \times \left[\eta^{(s)}\right]^3\right)$, $\eta^{(s)} = \sum_{q=1}^{Q^{(s)}} N^{(q)}$, because of the solution of two forward problems at each iteration, the burden reduces as s increases ($\eta^{(1)} = \eta^{(2)} = 841$ and $\eta^{(3)} = 805$ - Tab. I). Moreover, the multi-resolution implementations appear to be more effective than the bare approach because of the reduction of the total number of complex floating point operations to reach the convergence, $f_{pos} = \sum_{s=1}^{s_{opt}} \mathcal{O}\left(2 \times \left[\eta^{(s)}\right]^3\right) \times k_{opt}^{(s)}$ (Tab. II).

In the second experiment, the SNR value is varied from $20\,dB$ down to $5\,dB$ to further assess the robustness of the proposed approach as well as its ability to detect disconnected regions in the presence of high levels of noise. Thanks to this latter property and the consequent greater spatial resolution within the RoIs to which the actual scatterers belong, the reconstructions

with the multi-region strategy turn out to be better than those with the $IMSA-LS$ [Fig. 6(*a*) vs. Fig. 6(*c*) - $SNR = 10\,dB$ and Fig. 6(*b*) vs. Fig. 6(*d*) - $SNR = 5\,dB$] and almost insensitive to the blurring of the data except for the estimation of the support of the hollow square scatterer. As a matter of fact, it can be observed that the shapes of the actual objects are quite carefully reconstructed with the *IMSMRA-LS* while some difficulties occur in retrieving the hollow circular cylinder withe the *IMSA-LS*.

The third experiment deals with the sensitivity of the reconstruction to the target permittivity. Towards this end, the value of ε has been increased from 1.8 up to 4.0, while keeping the SNR equal to $20\,dB$. Figure 7 shows the inversion results when setting $\varepsilon = \varepsilon_a = 2.5$ [Fig. 7(*a*)-(*c*)], $\varepsilon = \varepsilon_a = 3.0$ [Fig. 7(*d*)-(*f*)], and $\varepsilon = \varepsilon_a = 4.0$ [Fig. 7(*g*)-(*i*)]. As it can be observed, the reconstructions worsen when the permittivity value increases. On the other hand, it should be also noticed that, until $\varepsilon_a \leq 4.0$, the results from the *IMSMRA-LS* turn out to be quite accurate and certainly better than those of the *IMSA-LS* and the *Bare-LS*. as further confirmed by the average values of the error indexes in Tab. III.

3.2 Analysis of the Resolution

The second test case deals with the different scattering scenario shown in Fig. 8 and composed by two objects of permittivity $\varepsilon = 1.8$, while the imaging setup has been kept equal to that of the previous example. In order to focus on the resolution of the multi-region approach, the minimum distance d between the objects has been varied in successive experiments from $d = 2.5\,\lambda$ down to $d = 0.1\,\lambda$ and the reconstructions [Figs. 8(*a*)-8(*d*)-8(*g*)-8(*l*)] have been compared with those from the standard multi-resolution approach [54] [Figs. 8(*b*)-8(*e*)-8(*h*)-8(*m*)] and the bare method [Figs. 8(*c*)-8(*f*)-8(*i*)-8(*n*)].

As expected, the *IMSMRA-LS* outperforms the *IMSA-LS* when the detection procedure allows one to distinguish the disconnected regions ($d > 0.9\lambda$). In such cases, the differences between the corresponding values of both the localization error δ and the support misfit Δ increases as the distance d enlarges (Fig. 9). Otherwise, both techniques achieve the same results still significantly better than those coming from the *Bare* technique as depicted in Fig. 8 (left column and center column versus right column) and confirmed by the values of the error indexes (Fig. 9).

It should be also noticed that the performances of the standard *LS* and *IMSA-LS* worsen as d increases, while the accuracy of the multi-region strategy appears to be almost constant. Concerning the minimum inter-objects distance ($d = 0.1\lambda$), the *IMSA* methods still improve the *LS* reconstruction because of the higher resolution achieved within the smallest *RoI* including the two actual scatterers.

These conclusions are also highlighted by the plots of the convergence values of the cost function (4) versus the object distance in Fig. 10. As it can be noticed, the enhanced resolution granted by the multi-region strategy results in a better matching with the scattering data. As an example, the case $d = 2.5\,\lambda$ corresponds to a convergence value $\Theta^{(s_{opt})}$ for the *IMSMR-LS* ($\Theta^{(s_{opt})}\Big|_{IMSA-LS} \approx 10^{-2}$) of about one order and two orders in magnitude lower than that of the *IMSA-LS* ($\Theta^{(s_{opt})}\Big|_{IMSA-LS} \approx 10^{-1}$) and the *Bare-LS* ($\Theta^{(s_{opt})}\Big|_{Bare-LS} \approx 10^{0}$), respectively.

3.3 Analysis of the Sensitivity to the *A-Priori* Information

With reference to the same scattering geometry of the test case in Sect. 3.2 and considering the distance $d = 2.5\,\lambda$, the third example is aimed at analyzing the dependence of the reconstruction accuracy on the knowledge of the permittivity of the scatterers. Towards this end, the reconstruction process has been initialized with a wrong *a-priori* information on the dielectric characteristics of the trial shape. More specifically, the permittivity of the objects has been assumed equal to $\varepsilon_a = 1.62$ and $\varepsilon_a = 1.98$ instead of $\varepsilon = 1.8$ (i.e., an underestimate and an overestimate of the actual value of about 10 %). Under these conditions the *LS*-based approaches have been applied and the reconstructions are shown in Fig. 11 along with the plots of Θ_k versus the iteration number (Fig. 12). Figure 11 confirms the same conclusions yielded from the analysis of Figs. 8(*a*)-8(*c*) and assesses the robustness of the multi-region approach not only with respect to data blurring, but also in the presence of an incorrect *a-priori* information. As it can be observed, the quality of the retrieved contours turns out to be very similar to that with an exact knowledge of the scatterer permittivity [Fig. 11(*a*) vs. Fig. 8(*a*)] as well as the convergence value of the cost function [Fig. 12(*a*) vs. Fig. 12(*b*) and Fig. 12(*c*)].

To further investigate on such a potential positive feature of the *IMSMR-LS*, the analysis has been extended from synthetic data to experimental measurements. Towards this end, the multiple-frequency angular-diversity bi-static dataset "*twodielTM_4f.exp*" of the *Marseille* repository

[61] has been considered as representative test case because of the presence of multiple disconnected and homogeneous scatterers. Such a benchmark is related to two off-centered homogeneous circular cylinders ($15\,mm$ in radius) having a nominal value of the object function equal to $\tau = 2.0$ and illuminated by a probing source from $V = 36$ different angular directions. For each view, the field samples have been collected at $M = 49$ measurement points in an aspect-limited configuration on a circle $\rho = 0.9\,m$ in radius. As regards the application of the inversion algorithms, the following parameters have been used: $L = 30\,cm$, $N^{(1)}_{IMSA} = 11 \times 11$ at $f = 2\,GHz$, $N^{(1)}_{IMSA} = 19 \times 19$ at $f = 4\,GHz$, and $N_{LS} = 41 \times 41$. The value of N_{LS} has been kept constant in order to perform a fair comparison in terms of spatial accuracy among *Bare* and *IMSA* approaches (i.e., similar spatial resolution within the RoIs).

Figures 13 and 14 show the results at the convergence when $f = 2\,GHz$ (Fig. 13) and $f = 4\,GHz$ (Fig. 14) with $\varepsilon_a = 3.0$ [Figs. 13(*a*)-13(*d*)-13(*g*) and Figs. 14(*a*)-14(*d*)-14(*g*)], $\varepsilon_a = 3.1$ [Figs. 13(*b*)-13(*e*)-13(*h*) and Figs. 14(*b*)-14(*e*)-14(*h*)], and $\varepsilon_a = 3.3$ [Figs. 13(*c*)-13(*f*)-13(*i*) and Figs. 14(*g*)-14(*h*)-14(*i*)]. The scatterers are quite carefully located and estimated at $f = 2\,GHz$ and for an accurate knowledge of the dielectric properties of the scatterers being $\varepsilon_a = 3.0$ [Figs. 13(*a*)-13(*d*)-13(*g*)], while non-negligible differences arise in correspondence with a higher frequency [$f = 4\,GHz$ - Figs. 14(*a*)-14(*d*)-14(*g*)]. The enhanced performances of the *IMSMR-LS* stand out in a more significant fashion when $\varepsilon_a = 3.1$. In such a case, the reconstructions worsen for both the *IMSA-LS* and the *Bare-LS*, especially when the frequency increases [$f = 4\,GHz$: Fig. 14(*d*) vs. Fig. 14(*e*) - *IMSA-LS*; Fig. 14(*g*) vs. Fig. 14(*h*) - *Bare-LS*]. Incidentally, the larger number of unknowns considered in the *Bare-LS* my explain it poor performance. On the contrary, the quality of the inversion turns out to be almost equivalent using the multiregion strategy [Fig. 13(*a*) vs. Fig. 13(*b*) - $f = 2\,GHz$; Fig. 14(*a*) vs. Fig. 14(*b*) - $f = 4\,GHz$]. Similar conclusions holds true also when $\varepsilon_a = 3.3$, even though the *IMSA-LS* reconstructions slightly improve [Fig. 13(*f*) vs. Fig. 13(*e*) - $f = 2\,GHz$; Fig. 14(*f*) vs. Fig. 14(*e*) - $f = 4\,GHz$].

4 Conclusions

In microwave imaging, an automatic procedure based on the integration of a multi-region approach and the level set optimization has been proposed to properly deal with the qualitative imaging (i.e., positions and shapes) of multiple scatterers. The method is characterized by an effective exploitation of the scattering data by means of the multi-region multi-scale representation that allows a smart allocation of the problem unknowns to enhance both detection properties and the spatial resolution in the *RoI*s where the unknown objects are supposed to be located.

The most significant methodological novelties of this work consist in:

- a multi-region level set representation nested into a multi-step architecture to properly deal with multiple shapes reconstruction, thus improving and generalizing the range of applicability of *LS* approaches;
- an innovative unsupervised object detection technique based on the theory of closed curves in discrete spaces;
- a new unsupervised termination criterion based on the use of the Hausdorff distance.

Thanks to the numerical assessment concerned with different scenarios and both synthetic and experimental data, the following main indications can be drawn:

- the *IMSMRA-LS* proved to give an always better or equivalent resolution of the *IMSA* single-region implementation and a non-negligible improvement over the bare *LS;*
- the multi-region strategy turned out less computationally-expensive than the standard *LS* approach and comparable (even though with an enhanced reconstruction efficiency) with the *IMSA-LS*.

Future developments will be aimed at extending the multi-region approach to the quantitative imaging (i.e., the reconstruction of the dielectric profiles of the scatterers) and three-dimensional geometries where a reduction of the computational costs and a high spatial resolution are not only useful, but mandatory. Concerning the latter item, it should be also pointed out that the proposed approach can be profitably used in conjunction with fast direct solvers further improving and multiplying its intrinsic positive features.

References

[1] P. J. Shull, *Nondestructive Evaluation: Theory, Techniques and Applications.* CRC Press, Boca Raton, 2002.

[2] H. Schubert and A. Kuznetsov, *Detection of Explosives and Landmines: Methods and Field Experience*. Kluwer Academic Pub., Boston, 2001.

[3] A. G. Webb, *Introduction to Biomedical Imaging*, IEEE Press Series on Biomedical Engineering. Wiley-IEEE Press, Hoboken, 2002.

[4] D. D. Ferris and N. C. Currie, "A survey of current technologies for through-wall-surveillance (TWS)," *Proc. SPIE*, vol. 3577, pp. 62-68, 1998.

[5] J. Ch. Bolomey, "Microwave imaging techniques for NDT and NDE," *Proc. Training Workshop on Advanced Microwave NDT/NDE Techniques*, Supelec/CNRS, Paris, Sept. 7-9, 1999.

[6] S. Kharkovsky and R. Zoughi, "Microwave and millimeter wave nondestructive testing and evaluation - Overview and recent advances," *IEEE Instrum. Meas. Mag.*, vol. 10, pp. 26-38, Apr. 2007.

[7] A. Abubakar, P. M. van den Berg, and J. J. Mallorqui, "Imaging of biomedical data using a multiplicative regularized contrast source inversion method," *IEEE Trans. Microw. Theory Tech.*, vol. 50, pp. 1761-1771, Jul. 2002.

[8] S. Caorsi, A. Massa, and M. Pastorino, "A computational technique based on a real-coded genetic algorithm for microwave imaging purposes ," *IEEE Trans. Geosci. Remote Sens.*, vol. 38, pp. 1697-1708, 2000.

[9] A. Massa, D. Franceschini, G. Franceschini, M. Pastorino, M. Raffetto, and M. Donelli, "Parallel GA-based approach for microwave imaging applications," *IEEE Trans. Antennas Propag.*, vol. 53, pp. 3118-3127, 2005.

[10] S. Caorsi, A. Massa, M. Pastorino, and A. Randazzo, "Electromagnetic detection of dielectric scatterers using phaseless synthetic and real data and the memetic algorithm," *IEEE Trans. Geosci. Remote Sens.*, vol. 41, pp. 2745-2753, 2003.

[11] M. Donelli and A. Massa, "Computational approach based on a particle swarm optimizer for microwave imaging of two-dimensional dielectric scatterers," *IEEE Trans. Microwave Theory Tech.*, vol. 53, no. 5, pp. 1761-1776, May 2005.

[12] M. Donelli, G. Franceschini, A. Martini, and A. Massa, "An integrated multiscaling strategy based on a particle swarm algorithm for inverse scattering problems," *IEEE Trans. Geosci. Remote Sens.*, vol. 44, pp. 298-312, 2006.

[13] A. Qing, "Dynamic differential evolution strategy and applications in electromagnetic inverse scattering problems," *IEEE Trans. Geosci. Remote Sens.*, vol. 44, pp. 116-125, 2006.

[14] Q. Dong and C. M. Rappaport, "Microwave subsurface imaging using direct finite-difference frequency-domain-based inversion," *IEEE Trans. Geosci. Remote Sensing*, vol. 47, pp. 3664-3670, Nov. 2009.

[15] L. Li, H. Zheng, and F. Li, "Two-dimensional contrast source inversion method with phaseless data: TM case," *IEEE Trans. Geosci. Remote Sensing*, vol. 47, pp. 1719-1736, Jun. 2009.

[16] J. De Zaeytijd, A. Franchois, C. Eyraud, and J. M. Geffrin, "Full-wave three-dimensional microwave imaging with a regularized gauss-newton method: theory and experiments," *IEEE Trans. Antennas Propag.*, vol. 55, pp. 3279-3292, Nov. 2007.

[17] M. Brignone, G. Bozza, A. Randazzo, M. Piana, and M. Pastorino, "A hybrid approach to 3D microwave imaging by using linear sampling and ACO," *IEEE Trans. Antennas Propag.*, vol. 56, pp. 3224-3232, 2008.

[18] M. Donelli, D. Franceschini, P. Rocca, and A. Massa, "Three-dimensional microwave imaging problems solved through an efficient multiscaling particle swarm optimization," *IEEE Trans. Geosci. Remote Sens.*, vol. 47, pp. 1467-1481, 2009.

[19] H. Zhou, T. Takenaka, J. Johnson, and T. Tanaka, "Breast imaging model using microwaves and a time domain three dimensional reconstruction method," *Progress In Electromagnetics Research*, vol. 93, pp. 57-70, 2009.

[20] R. Solimene, F. Soldovieri, G. Prisco, and R. Pierri, "Three-dimensional through-wall imaging under ambiguous wall parameters," *IEEE Trans. Geosci. Remote Sensing*, vol. 47, pp. 1310-1317, May 2009.

[21] T. Rubk, P. M. Meaney, P. Meincke, and K. D. Paulsen, "Nonlinear microwave imaging for breast-cancer screening using gauss-newton's method and the CGLS inversion algorithm," *IEEE Trans. Antennas Propagat.*, vol. 55, pp. 2320-2331, Aug. 2007.

[22] F. Soldovieri, R. Solimene, and G. Prisco, "A multiarray tomographic approach for through-wall imaging," *IEEE Trans. Geosci. Remote Sensing*, vol. 46, pp. 1192-1199, Apr. 2008.

[23] O. M. Bucci and T. Isernia, "Electromagnetic inverse scattering: retrievable information and measurement strategies," *Radio Sci.*, vol. 32, pp. 2123-2138, Nov.-Dec. 1997.

[24] M. Bertero and P. Boccacci, *Introduction to Inverse Problems in Imaging*. IOP Publishing Ltd, Bristol, 1998.

[25] O. M. Bucci and G. Franceschetti, "On the spatial bandwidth of scattered fields," *IEEE Trans. Antennas Propagat.*, vol. 35, no. 12, pp. 1445-1455, Dec. 1987.

[26] T. Isernia, V. Pascazio, and R. Pierri, "On the local minima in a tomographic imaging technique," *IEEE Trans. Antennas Propagat.*, vol. 39, no. 7, pp. 1696-1607, Jul. 2001.

[27] O. M. Bucci, L. Crocco, T. Isernia, and V. Pascazio, "Subsurface inverse scattering problems: quantifying, qualifying, and achieving the available information," *IEEE Trans. Geosci. Remote Sensing*, vol. 39, pp. 2527-2537, Nov. 2001.

[28] E. L. Miller and A. S. Willsky, "A multiscale, statistically based inversion scheme for linearized inverse scattering problems," *IEEE Trans. Antennas Propag.*, vol. 34, no. 2, pp. 346-357, Mar. 1996.

[29] A. Baussard, E. L. Miller, and D. Lesselier, "Adaptive muliscale reconstruction of buried objects," *Inverse Problems*, vol. 20, pp. S1-S15, Dec. 2004.

[30] S. Caorsi, M. Donelli, and A. Massa, "Detection, location, and imaging of multiple scatterers by means of the iterative multiscaling method," *IEEE Trans. Microwave Theory Tech.*, vol. 52, no. 4, pp. 1217-1228, Apr. 2004.

[31] G. Franceschini, M. Donelli, R. Azaro, and A. Massa, "Inversion of phaseless total field data using a two-step strategy based on the iterative multiscaling approach," *IEEE Trans. Geosci. Remote Sens.*, vol. 44, pp. 3527-3539, 2006.

[32] A. Litman, "Reconstruction by level sets of *n*-ary scattering obstacles," *Inverse Problems*, vol. 21, pp. S131-S152, Dec. 2005.

[33] W. C. Chew, *Waves and Fields in Inhomogeneous Media*. IEEE Press, Psicataway, 1995.

[34] A. Bréard, G. Perrusson, and D. Lesselier, "Hybrid differential evolution and retrieval of buried spheres in subsoil," *IEEE Geosci. Remote Sens. Lett.*, vol. 5, pp. 788-792, 2008.

[35] S. Caorsi, A. Massa, M. Pastorino, and M. Donelli, "Improved microwave imaging procedure for nondestructive evaluations of two-dimensional structures," *IEEE Trans. Antennas Propag.*, vol. 52, pp. 1386-1397, Jun. 2004.

[36] M. Benedetti, M. Donelli, and A. Massa, "Multicrack detection in two-dimensional structures by means of GA-based strategies," *IEEE Trans. Antennas Propag.*, vol. 55, no. 1, pp. 205-215, Jan. 2007.

[37] V. Cingoski, N. Kowata, K. Kaneda, and H. Yamashita, "Inverse shape optimization using dynamically adjustable genetic algorithms," *IEEE Trans. Energ. Convers.*, vol. 14, no. 3, pp. 661-666, Sept. 1999.

[38] I. T. Rekanos, "Shape reconstruction of a perfectly conducting scatterer using differential evolution and particle swarm optimization," *IEEE Trans. Geosci. Remote Sensing*, vol. 46, pp. 1967-1974, Jul. 2008.

[39] J. Cea, S. Garreau, P. Guillame, and M. Masmoudi, "The shape and topological optimizations connection," *Comput. Methods Appl. Mech. Eng.*, vol. 188, no. 4, pp. 713-726, 2000.

[40] M. Masmoudi, J. Pommier, and B. Samet, “The topological asymptotic expansion for the Maxwell equations and some applications,” *Inverse Problems*, vol. 21, pp. 547-564, Apr. 2005.

[41] S. Osher and J. A. Sethian, “Fronts propagating with curvature-dependent speed: algorithms based on Hamilton-Jacobi formulations,” *J. Comput. Phys.*, 79, pp. 12-49, Nov. 1988.

[42] J. A. Sethian, *Level Set and Fast Marching Methods*. Cambridge University Press, Cambridge, UK, 2nd ed., 1999.

[43] F. Santosa, “A level-set approach for inverse problems involving obstacles,” *ESAIM: COCV*, vol. 1, pp. 17-33, Jan. 1996.

[44] O. Dorn and D. Lesselier, “Level set methods for inverse scattering,” *Inverse Problems*, vol. 22, pp. R67-R131, Aug. 2006.

[45] A. Litman, D. Lesselier, and F. Santosa, "Reconstruction of a two-dimensional binary obstacle by controlled evolution of a level-set," *Inverse Problems*, vol. 14, pp. 685-706, Jun. 1998.

[46] R. Ferraye, J. Y. Dauvignac, and Ch. Pichot, “Reconstruction of complex and multiple shape object contours using a level set method,” *J. Electromagn. Waves Applic.*, vol. 17, pp. 153-181, 2003.

[47] R. Ferraye, J. Y. Dauvignac, and Ch. Pichot, “An inverse scattering method based on contour deformations by means of a level set method using frequency hopping technique,” *IEEE Trans. Antennas Propagat.*, vol. 51, pp. 1100-1113, May 2003.

[48] M. R. Hajihashemi and M. El-Shenawee, “Shape reconstruction using the level set method for microwave applications,” *IEEE Antennas Wireless Propag. Lett.*, vol. 7, pp. 92-96, 2008.

[49] L. Souriau, B. Duchene, D. Lesselier, and R. E. Kleinman, “Modified gradient approach to inverse scattering for binary objects in stratified media,” Inverse Problems, vol. 12, pp. 463-481, 1996.

[50] I. T. Rekanos and T. D. Tsiboukis, "An inverse scattering technique for microwave imaging of binary objects," *IEEE Trans. Microwave Theory Tech.*, vol. 50, pp. 1439-1441, May 2002.

[51] F. Cakoni and D. Colton, *Qualitative Methods in Inverse Scattering Theory*. Springer, Berlin, 2006.

[52] R. Aramini, M. Brignone, and M. Piana, "The linear sampling method without sampling," *Inverse Problems*, vol. 22, pp. 2237-2254, 2006.

[53] A. Kirsch and N. Grinberg, *The Factorization Method for Inverse Problems*. Oxford University Press Inc., New York, 2008.

[54] M. Benedetti, D. Lesselier, M. Lambert, and A. Massa, "A multi-resolution technique based on shape optimization for the reconstruction of homogeneous dielectric objects," *Inverse Problems*, vol. 25, pp. 1-26, Jan. 2009.

[55] D. Colton and R. Kress, *Inverse Acoustic and Electromagnetic Scattering Theory*, 2nd Edition. Springer, Berlin, 1998.

[56] D. P. Huttenlocher, G. A. Klanderman, and W. J. Rucklidge, "Comparing images using the Hausdorff distance," *IEEE Trans. Pattern Analysis and Machine Intelligence*, vol. 15, pp. 850-863, Sep. 1993.

[57] D.-G. Sim, O.-K. Kwon, and R.-H. Park, "Object matching algorithms using robust Hausdorff distance measures," *IEEE Trans. Image Processing*, vol. 8, pp. 425-429, Mar. 1999.

[58] J. P. Bustos, F. Donoso, A. Guesalaga, and M. Torres, "Matching radar and satellite images for ship trajectory estimation using the Hausdorff distance," *IET Radar Sonar Navigation*, vol. 1, pp. 50-58, Feb. 2007.

[59] P. Gastaldo and R. Zunino, "Hausdorff distance for robust and adaptive template selection in visual target detection," *Electron. Lett.*, vol. 38, pp. 1651-1653, Dec. 2002.

[60] G. Thürmer, "Closed curves in n-dimensional discrete space," *Graphical Models*, vol. 65, pp. 43-60, Jan. 2003.

[61] K. Belkebir and M. Saillard, "Testing inversion algorithms against experimental data," *Inverse Problems*, vol. 17, pp. 1565-1702, Dec. 2001.

FIGURE CAPTIONS

- **Figure 1.** Problem geometry.
- **Figure 2.** *IMSMR-LS*: (*a*) descriptive parameters of a *RoI* and (*b*) *RoI* detection procedure.
- **Figure 3.** *IMSMR-LS - Numerical Assessment* ("Three objects" - $\varepsilon = \varepsilon_a = 1.8$, $L = 5\lambda$, $SNR = 20\,dB$). Inversion results at (*a*) $s = 1$, (*c*) $s = 2$, and (*e*) $s = s_{opt} = 3$. Plot of the level set function: (*b*) $\phi^{(1)}$, (*d*) $\phi^{(2)}$, and (*f*) $\phi^{(3)}$.
- **Figure 4.** *IMSMR-LS - Numerical Assessment* ("Three objects" - $\varepsilon = \varepsilon_a = 1.8$, $L = 5\lambda$, $SNR = 20\,dB$). Behavior of the cost function Θ_k versus k.
- **Figure 5.** *IMSMR-LS - Comparative Analysis* ("Three objects" - $\varepsilon = \varepsilon_a = 1.8$, $L = 5\lambda$, $SNR = 20\,dB$). Inversion results obtained with (*a*)(*b*) the *IMSA-LS* ($s_{opt} = 1$) and (*c*)(*d*) the *Bare-LS*: (*a*)(*c*) reconstructions and (*b*)(*d*) plot of the level set function.
- **Figure 6.** *IMSMR-LS - Robustness Analysis* ("Three objects" - $\varepsilon = \varepsilon_a = 1.8$, $L = 5\lambda$). Object supports estimated at the convergence by (*a*)(*b*) the *IMSMRA-LS* and (*c*)(*d*) the *IMSA-LS* in correspondence with blurred data characterized by a SNR value equal to (*a*)(*c*) $SNR = 10\,dB$ and (*b*)(*d*) $SNR = 5\,dB$.
- **Figure 7.** *IMSMR-LS - Robustness Analysis* ("Three objects", $L = 5\lambda$, $SNR = 20\,dB$). Inversion results obtained at the convergence by (*a*)(*d*)(*g*) *IMSMRA-LS*, (*b*)(*e*)(*h*) *IMSA-LS*, and (*c*)(*f*)(*i*) *Bare-LS* when (*a*)(*b*)(*c*) $\varepsilon = \varepsilon_a = 2.5$, (*d*)(*e*)(*f*) $\varepsilon = \varepsilon_a = 3.0$, and (*g*)(*h*)(*i*) $\varepsilon = \varepsilon_a = 4.0$.
- **Figure 8.** *IMSMR-LS - Resolution Analysis* ("Two objects" - $\varepsilon = \varepsilon_a = 1.8$, $L = 5\lambda$, $SNR = 20\,dB$). Reconstructed shapes with (*a*)(*d*)(*g*)(*l*) the *IMSMRA-LS*, (*b*)(*e*)(*h*)(*m*) the *IMSA-LS*, and (*c*)(*f*)(*i*)(*n*) the *Bare-LS* when (*a*)(*b*)(*c*) $d = 2.5\,\lambda$, (*d*)(*e*)(*f*) $d = 1.7\,\lambda$, (*g*)(*h*)(*i*) $d = 0.9\,\lambda$, and (*l*)(*m*)(*n*) $d = 0.1\,\lambda$.

- **Figure 9.** *IMSMR-LS - Resolution Analysis* ("Two objects" - $\varepsilon = \varepsilon_a = 1.8$, $L = 5\lambda$, $SNR = 20\,dB$). Localization error δ (*a*)(*c*) and area error Δ (*b*)(*d*) versus d.

- **Figure 10.** *IMSMR-LS - Resolution Analysis* ("Two objects" - $\varepsilon = \varepsilon_a = 1.8$, $L = 5\lambda$, $SNR = 20\,dB$). Value of the cost function at the convergence ($s = s_{opt}$) versus $\frac{d}{\lambda}$.

- **Figure 11.** *IMSMR-LS - Sensitivity Analysis* ("Two objects" - $\varepsilon = 1.8$, $L = 5\lambda$, $SNR = 20\,dB$). Reconstructions when using (*a*)(*b*) the *IMSMRA-LS*, (*c*)(*d*) the *IMSA-LS*, and (*e*)(*f*) *Bare-LS* when (*a*)(*c*)(*e*) $\varepsilon_a = 1.62$ and (*d*)(*e*)(*f*) $\varepsilon_a = 1.98$.

- **Figure 12.** *IMSMR-LS - Sensitivity Analysis* ("Two objects" - $\varepsilon = 1.8$, $L = 5\lambda$, $SNR = 20\,dB$). Plot of the cost function Θ_k versus k when (*a*) $\varepsilon_a = 1.8$, (*b*) $\varepsilon_a = 1.62$, (*c*) $\varepsilon_a = 1.98$.

- **Figure 13.** *IMSMR-LS - Experimental Data* ("twodielTM_4f.exp" - Dataset "Marseille" [61] - $f = 2\,GHz$). Reconstructions with (*a*)(*b*)(*c*) the *IMSMRA-LS*, (*d*)(*e*)(*f*) the *IMSA-LS*, and (*g*)(*h*)(*i*) the *Bare-LS* when (*a*)(*d*)(*g*) $\varepsilon_a = 3.0$, (*b*)(*e*)(*h*) $\varepsilon_a = 3.1$, and (*c*)(*f*)(*i*) $\varepsilon_a = 3.3$.

- **Figure 14.** *IMSMR-LS - Experimental Data* ("twodielTM_4f.exp" - Dataset "Marseille" [61] - $f = 4\,GHz$). Reconstructions with (*a*)(*b*)(*c*) the *IMSMRA-LS*, (*d*)(*e*)(*f*) the *IMSA-LS*, and (*g*)(*h*)(*i*) the *Bare-LS* when (*a*)(*d*)(*g*) $\varepsilon_a = 3.0$, (*b*)(*e*)(*h*) $\varepsilon_a = 3.1$, and (*c*)(*f*)(*i*) $\varepsilon_a = 3.3$.

TABLE CAPTIONS

- **Table I.** *Comparative Analysis* ("Three objects" - $\varepsilon = \varepsilon_a = 1.8$, $L = 5\lambda$, $SNR = 20\,dB$). Reconstruction errors.

- **Table II.** *Comparative Analysis* ("Three objects" - $\varepsilon = \varepsilon_a = 1.8$, $L = 5\lambda$, $SNR = 20\,dB$). Computational indexes.

- **Table III.** *Robustness Analysis* ("Three objects", $L = 5\lambda$, $SNR = 20\,dB$). Summary of the averaged reconstruction errors.

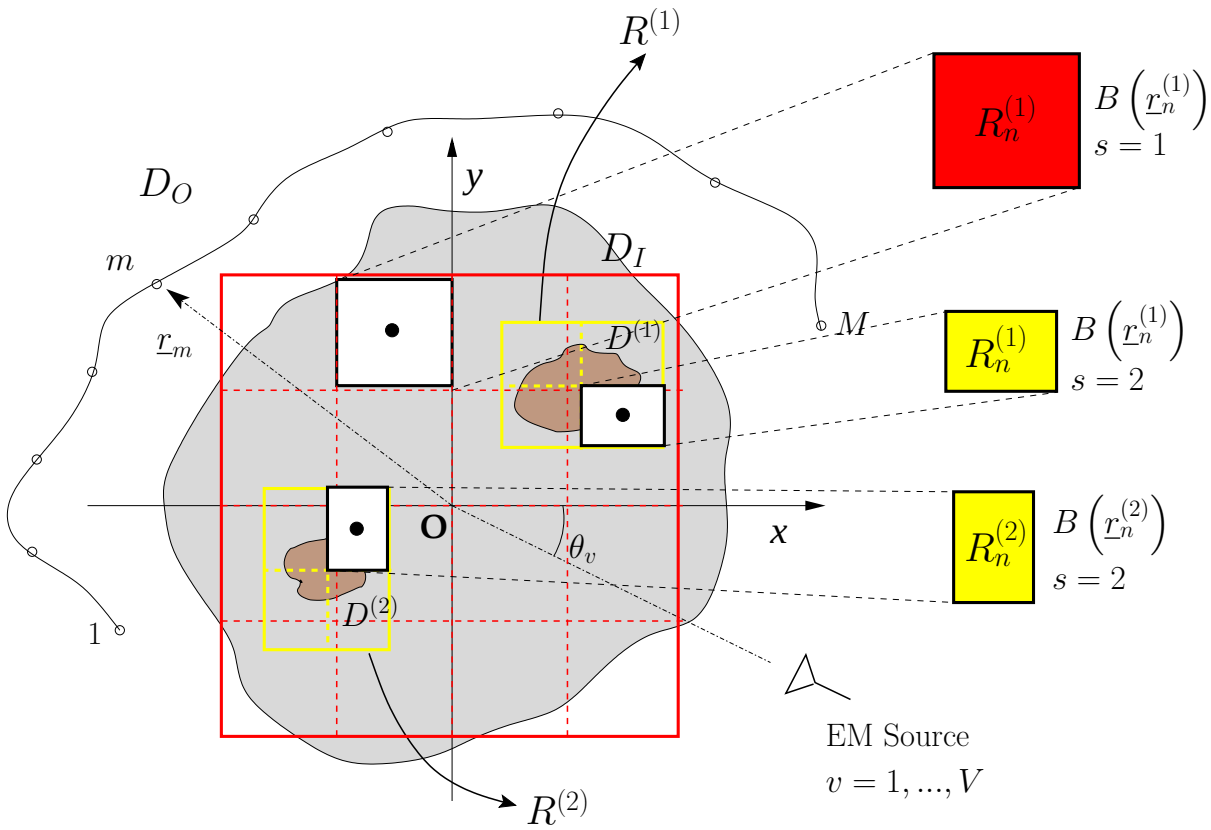

Figure 1 - M. Benedetti *et al.* - "Multiple shapes reconstruction ..."

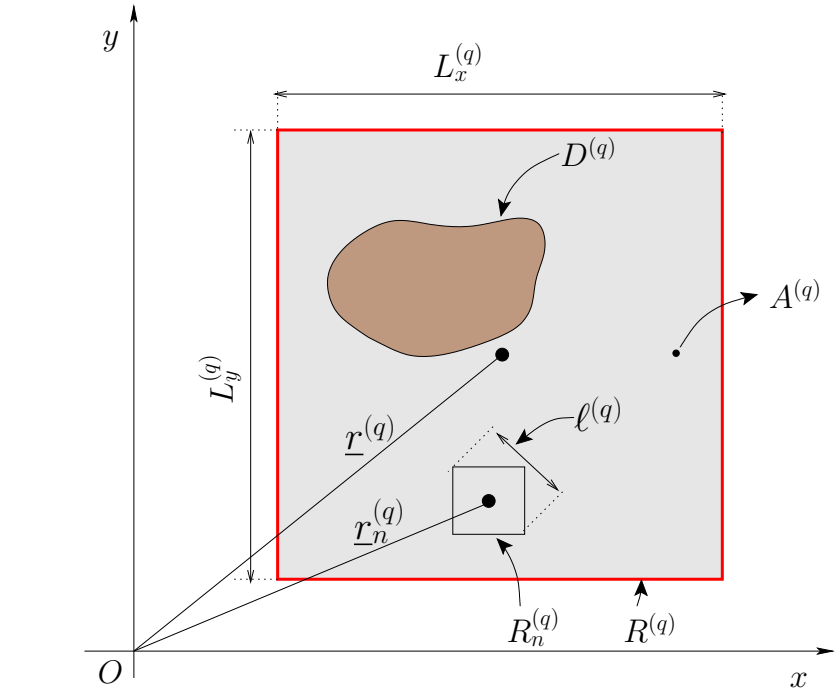

(*a*)

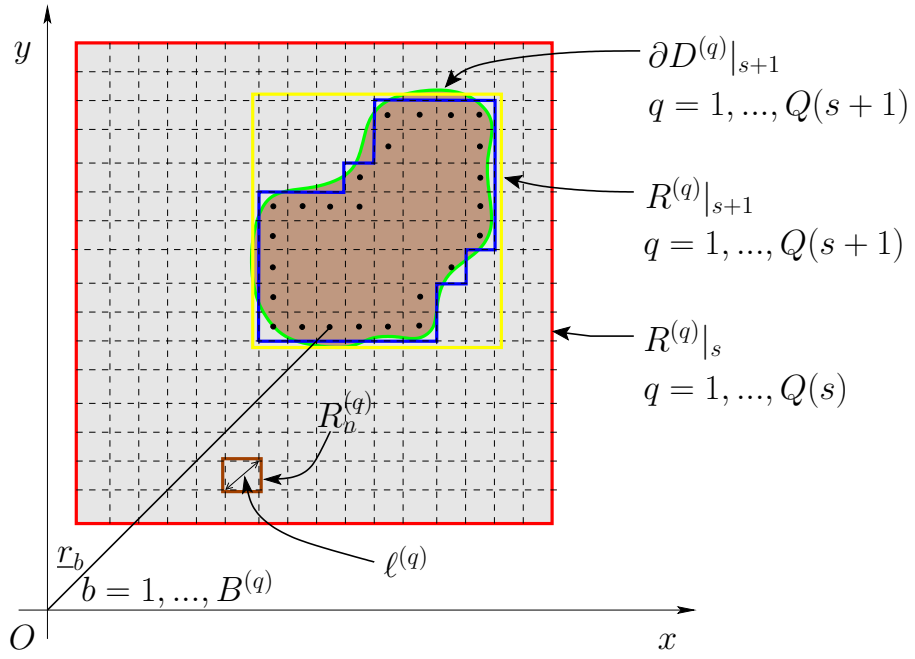

(*b*)

Figure 2 - M. Benedetti *et al.* - "Multiple shapes reconstruction ..."

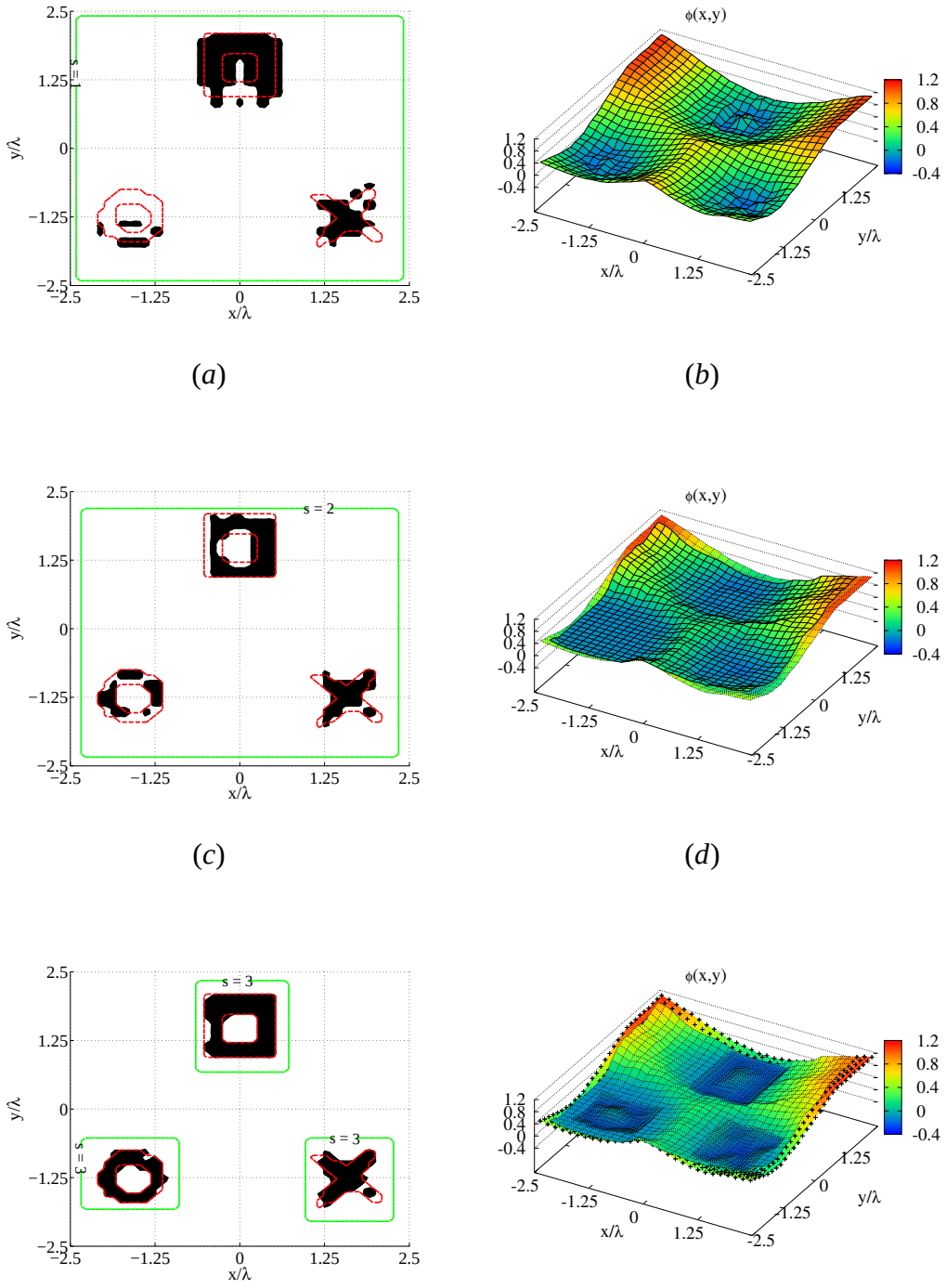

Figure 3 - M. Benedetti *et al.* - "Multiple shapes reconstruction ..."

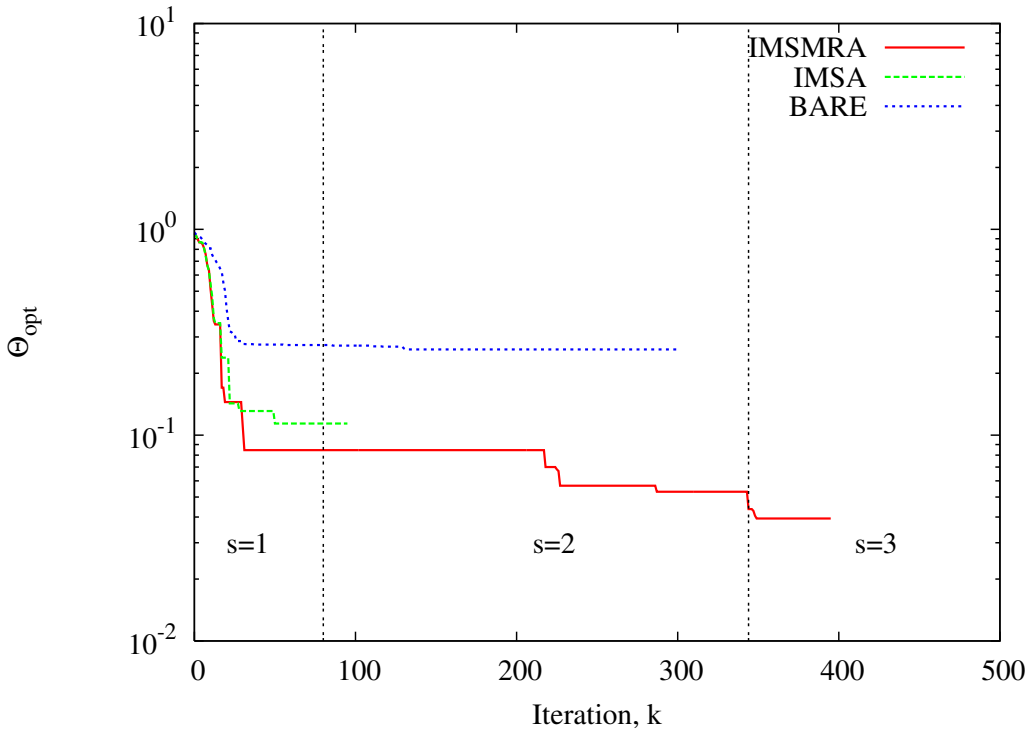

Figure 4 - M. Benedetti *et al.* - "Multiple shapes reconstruction ..."

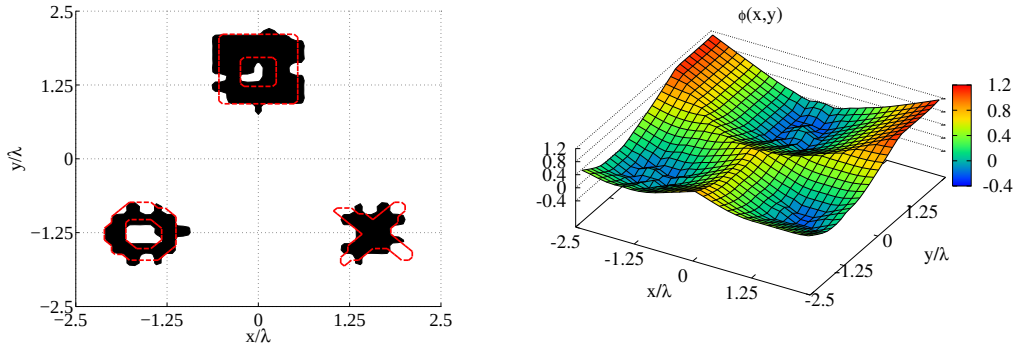

(*a*) (*b*)

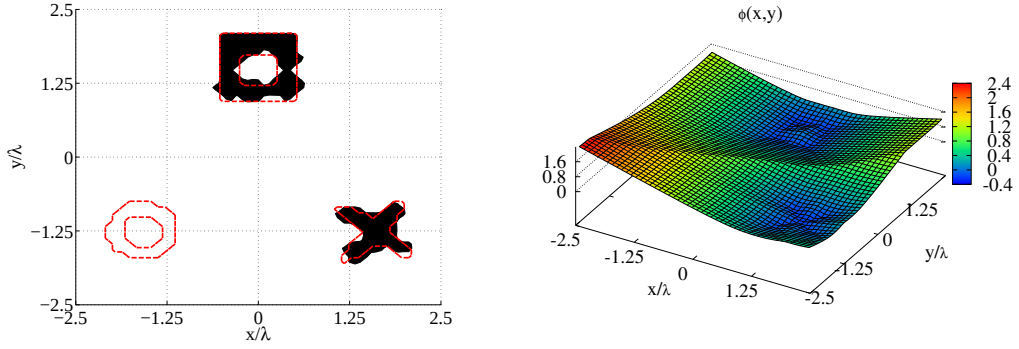

(*c*) (*d*)

Figure 5 - M. Benedetti *et al.* - "Multiple shapes reconstruction ..."

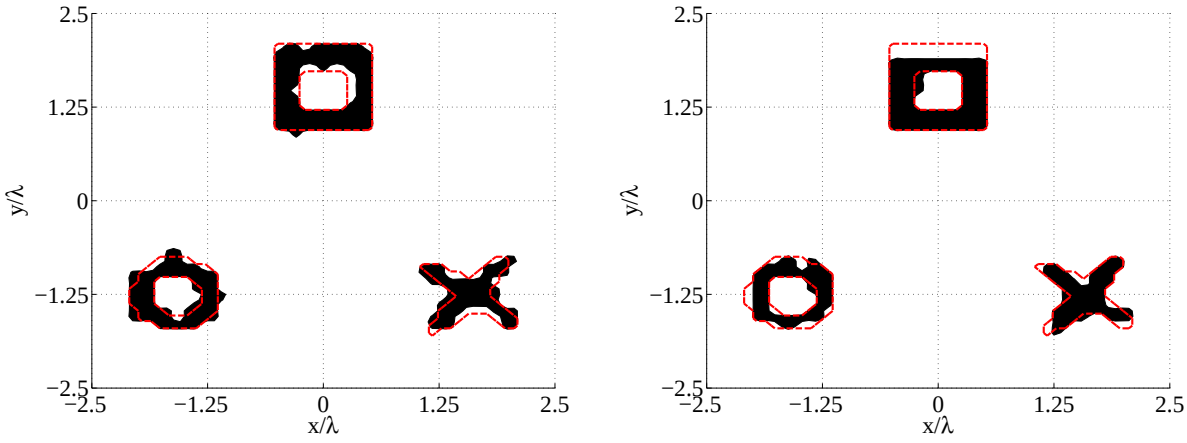

(*a*) (*b*)

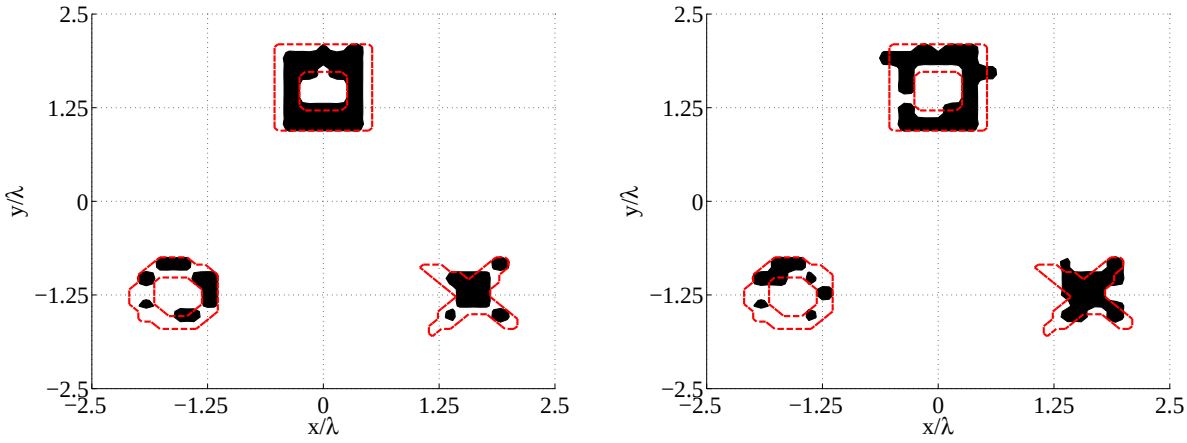

(*c*) (*d*)

Figure 6 - M. Benedetti *et al.* - "Multiple shapes reconstruction ..."

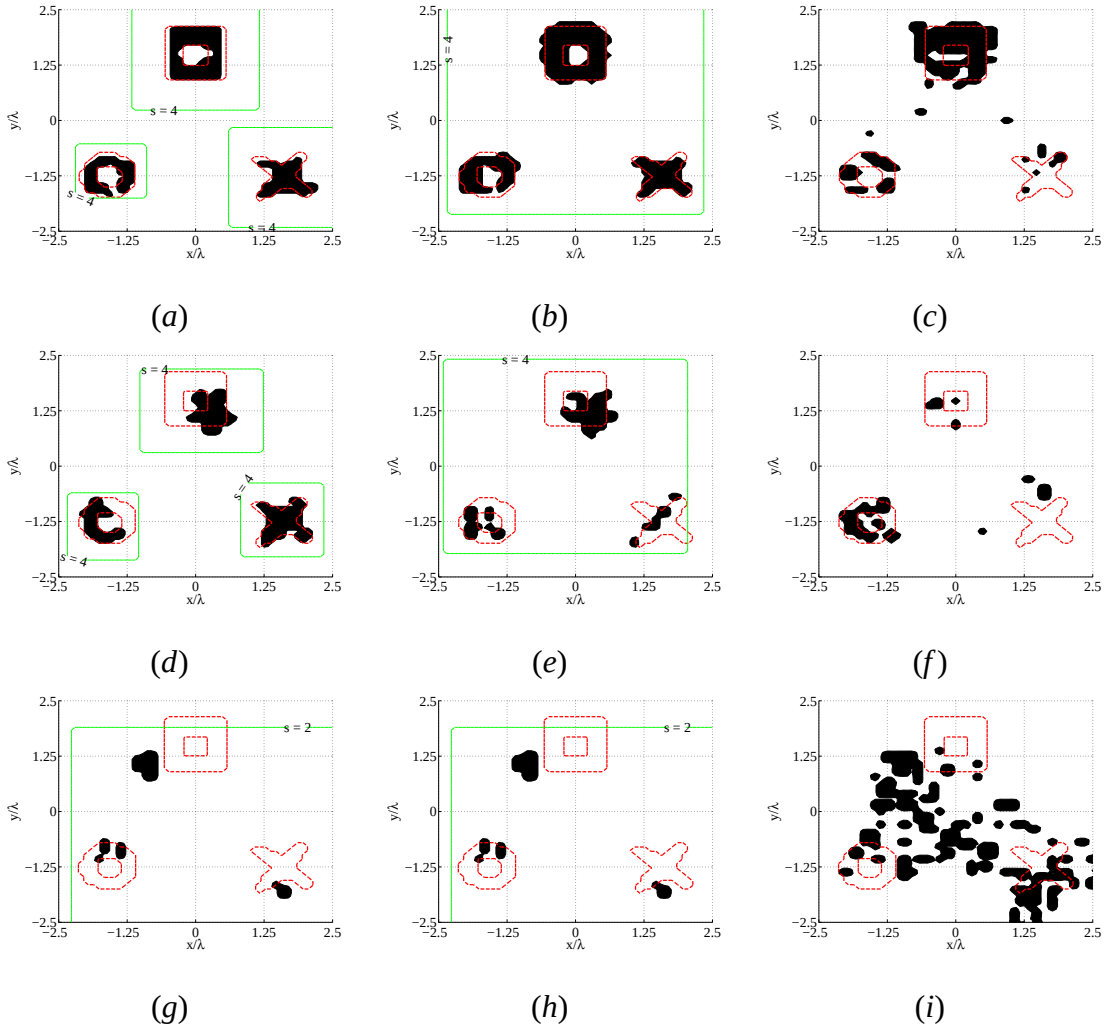

Figure 7 - M. Benedetti *et al.* - "Multiple shapes reconstruction ..."

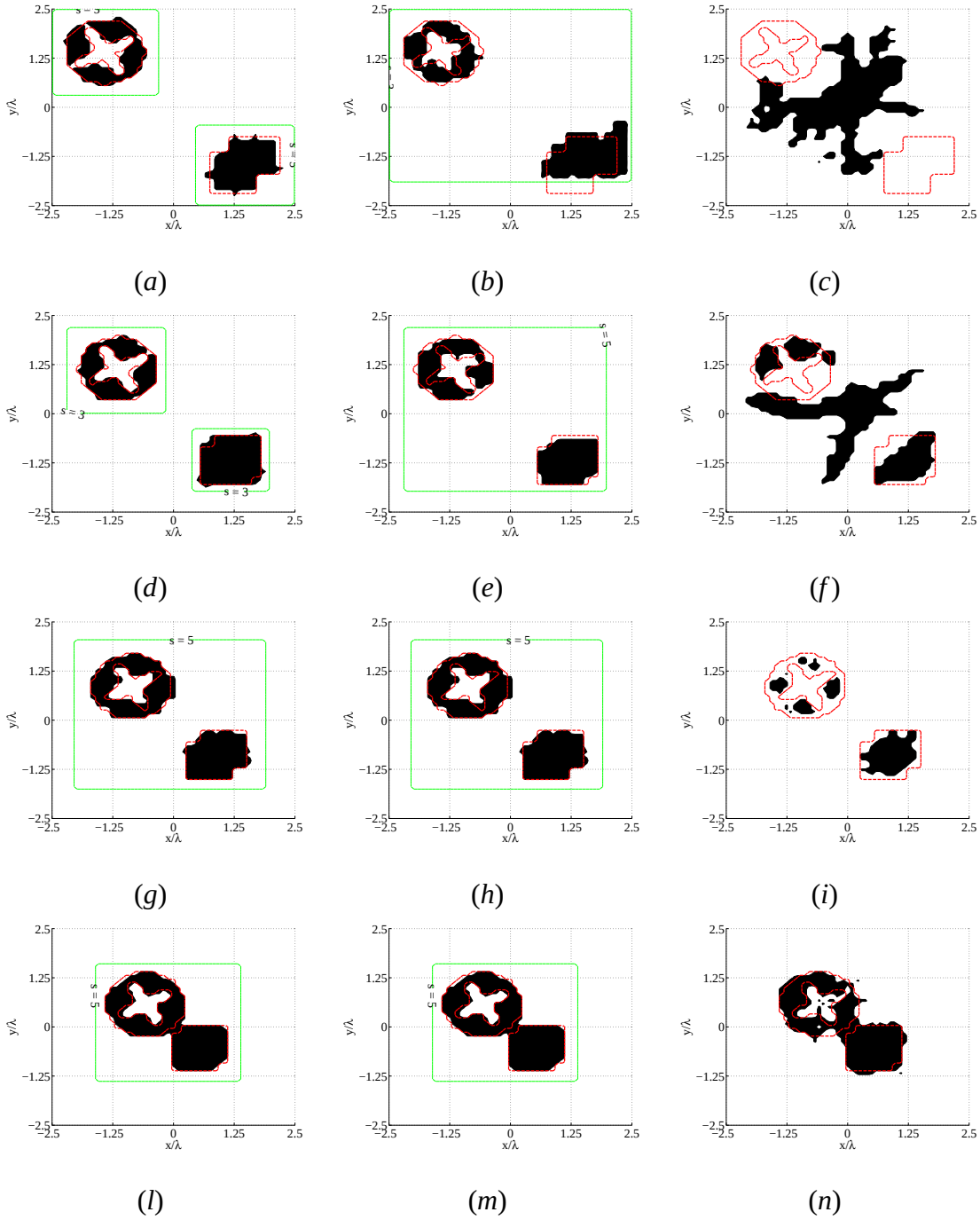

Figure 8 - M. Benedetti *et al.* - "Multiple shapes reconstruction ..."

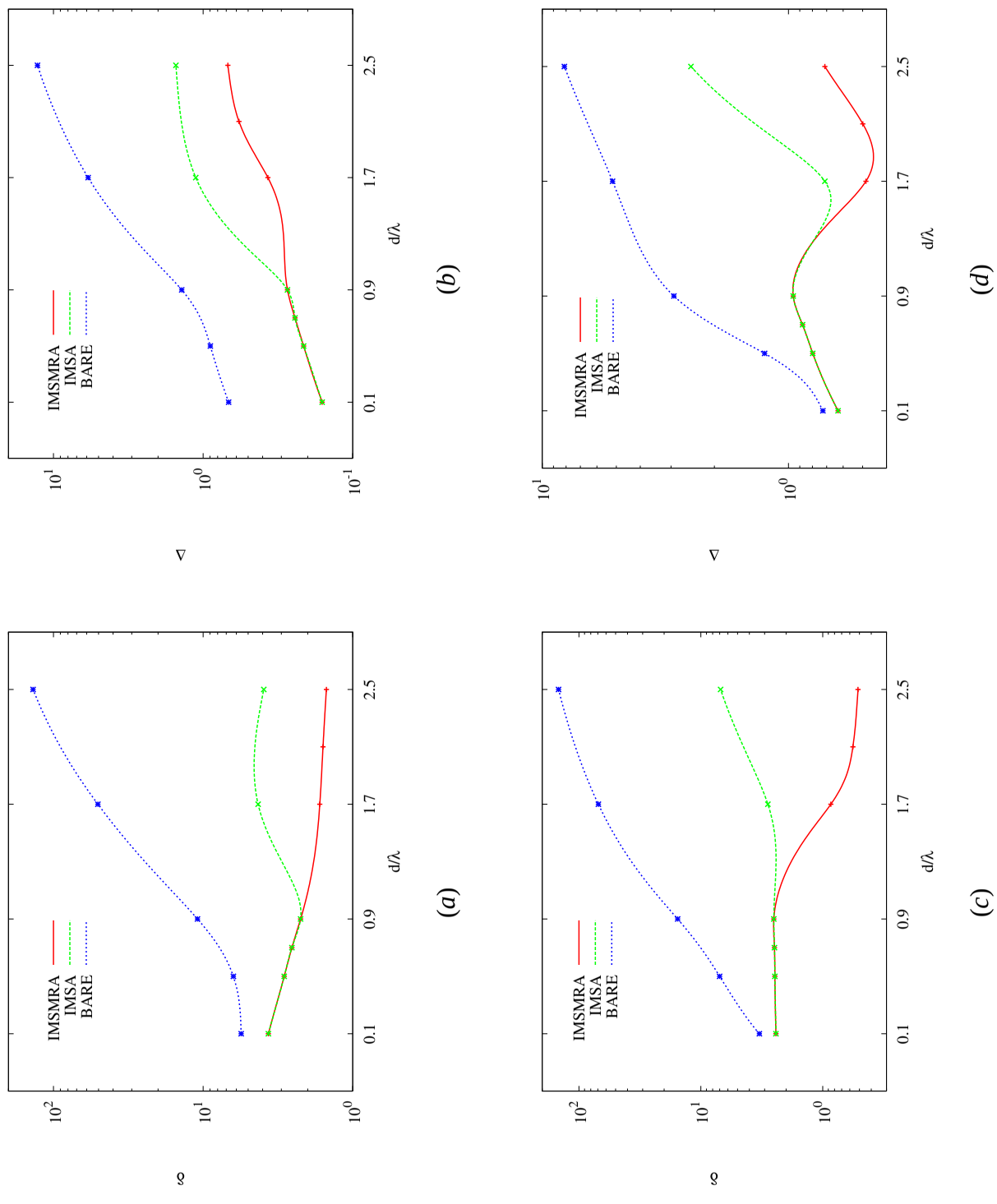

Figure 9 - M. Benedetti *et al.* - “Multiple shapes reconstruction ...“

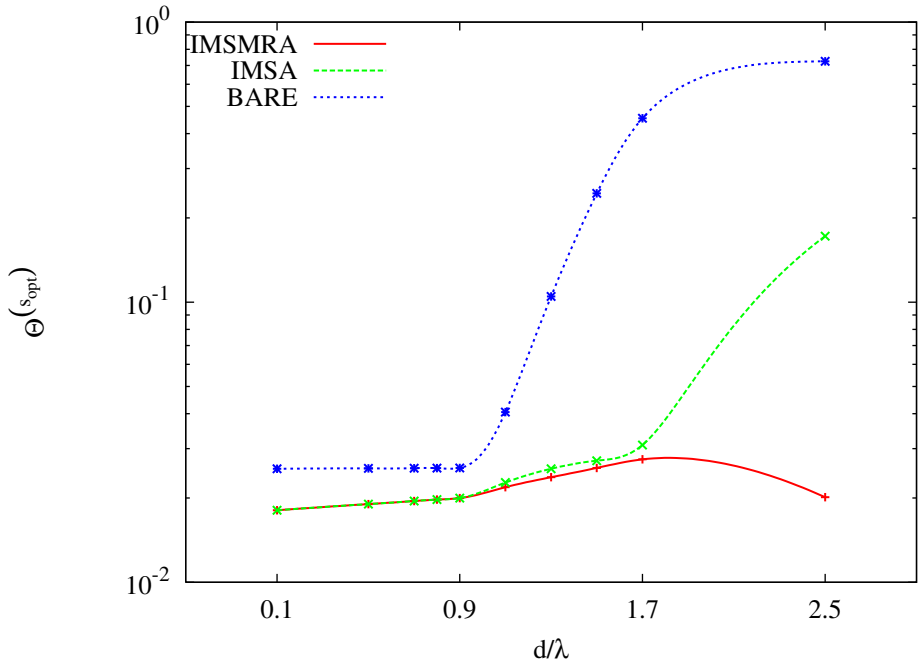

Figure 10 - M. Benedetti *et al.* - "Multiple shapes reconstruction ..."

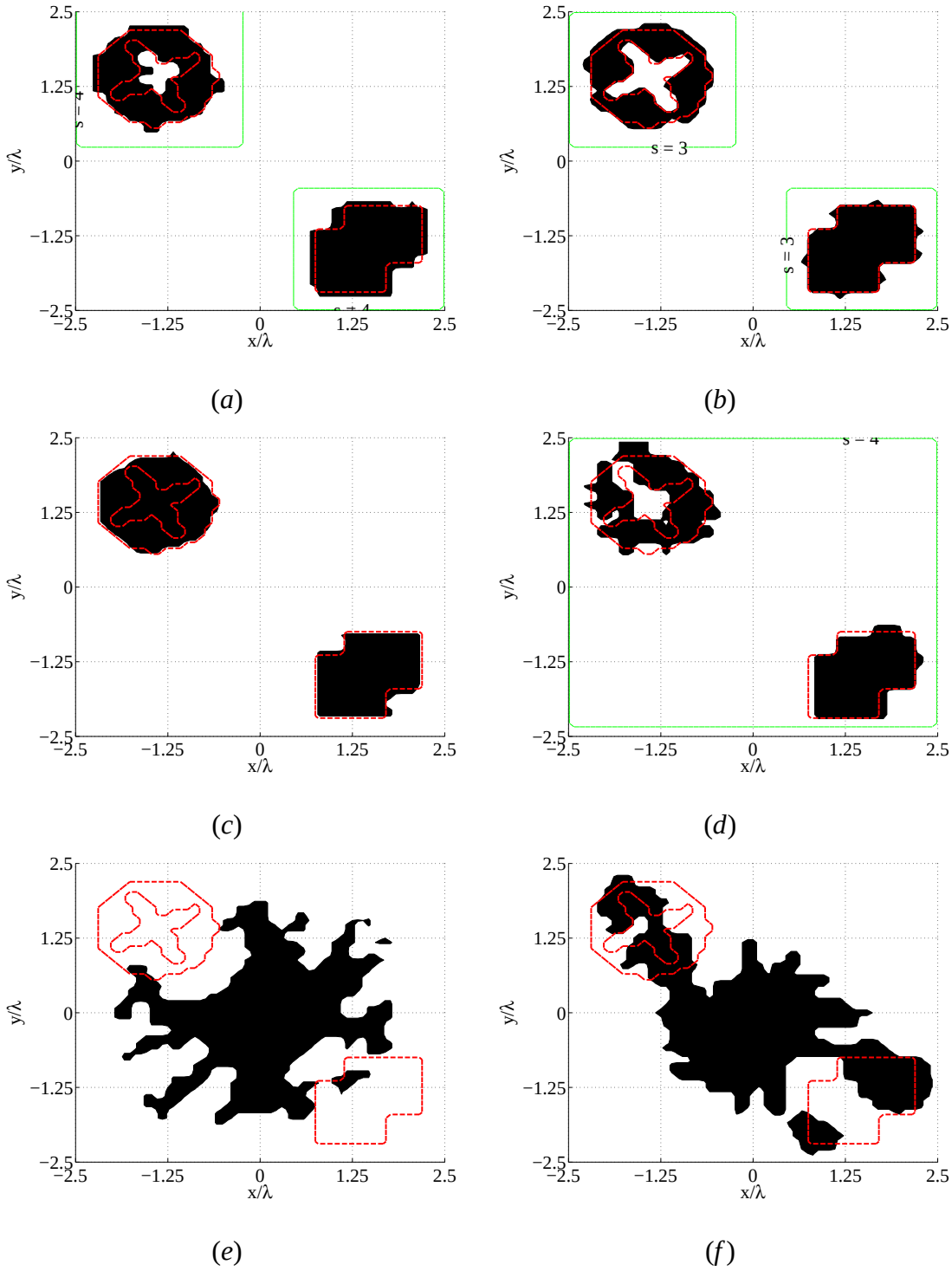

Figure 11 - M. Benedetti *et al.* - "Multiple shapes reconstruction ..."

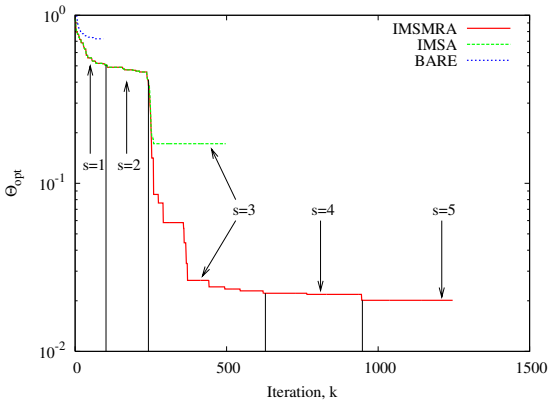

(*a*)

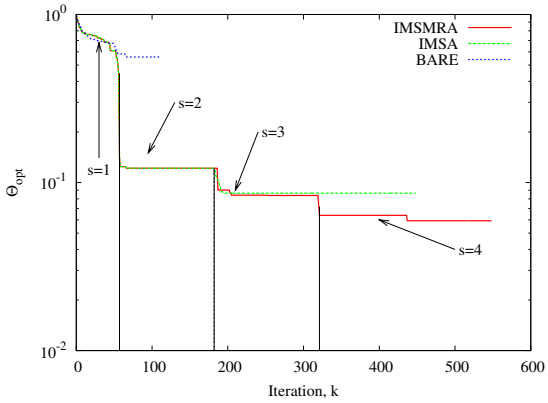

(*b*)

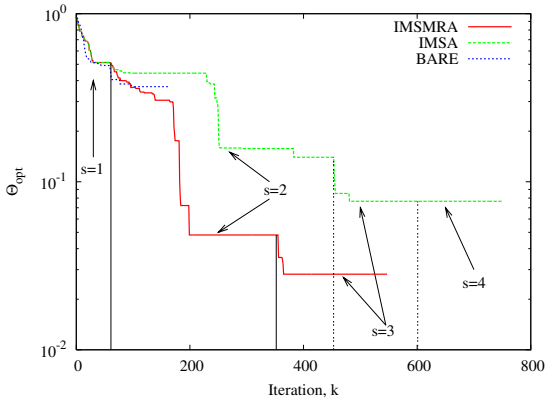

(*c*)

Figure 12 - M. Benedetti *et al.* - "Multiple shapes reconstruction ..."

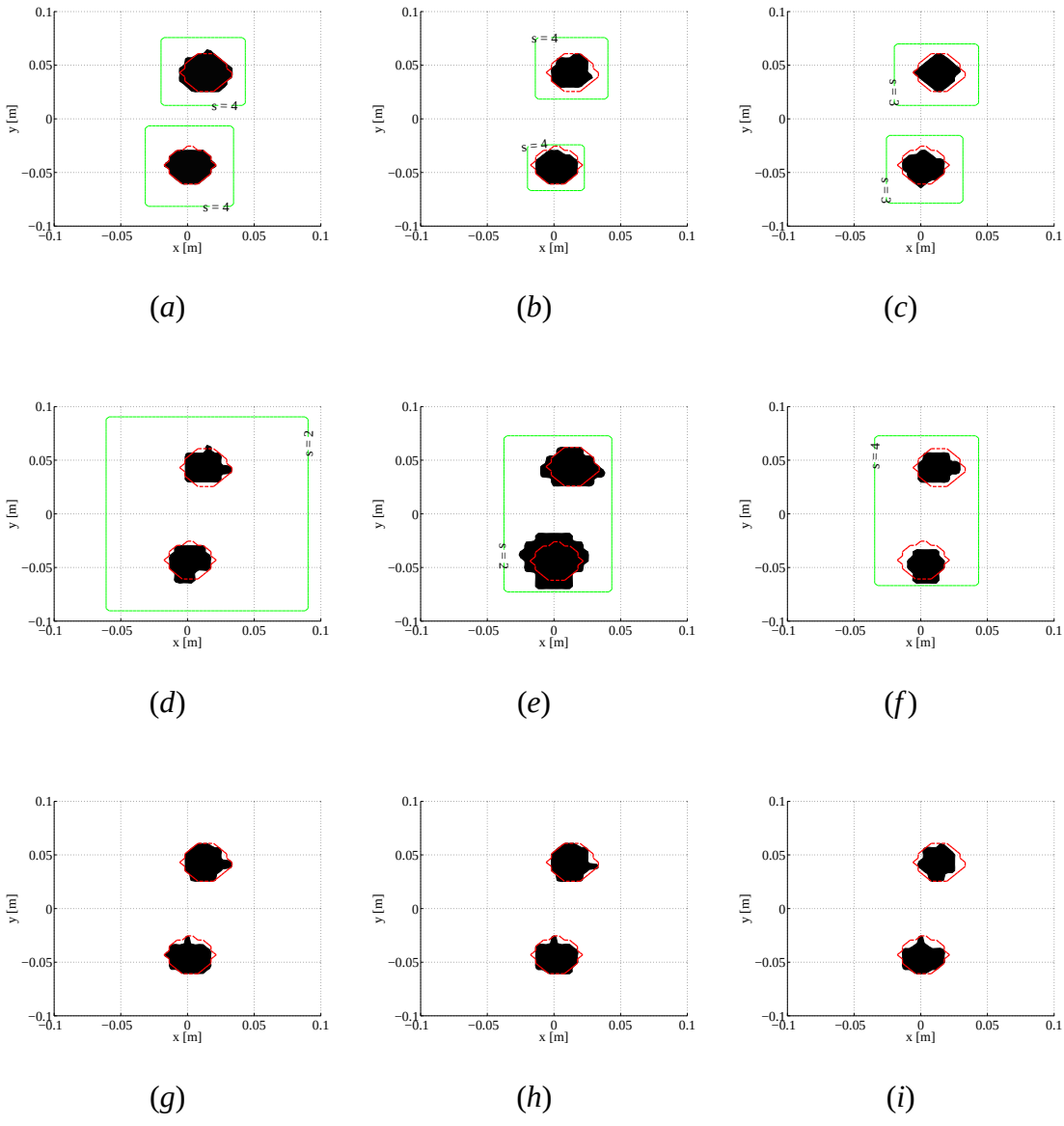

Figure 13 - M. Benedetti *et al.* - “Multiple shapes reconstruction ...“

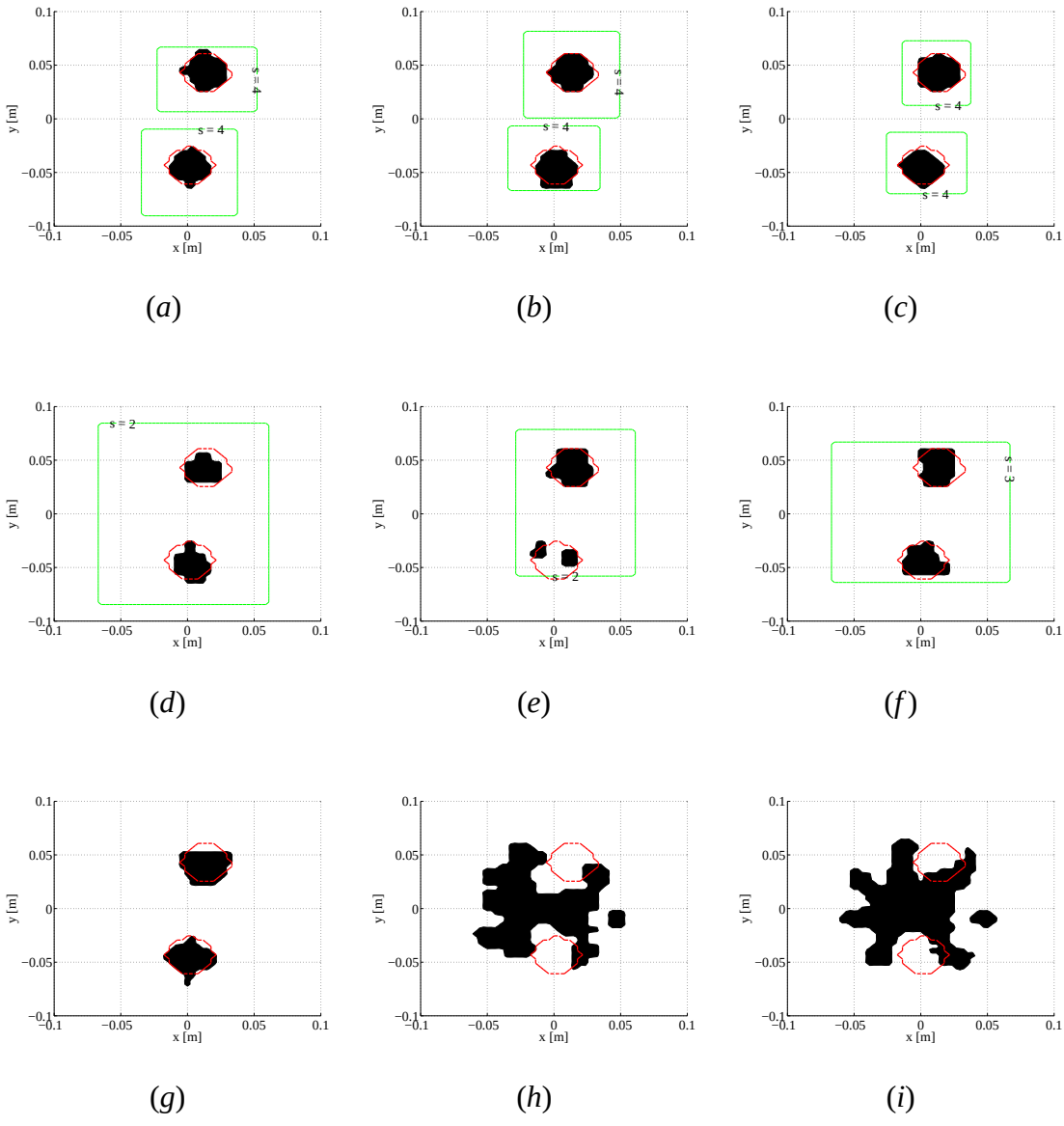

Figure 14 - M. Benedetti *et al.* - “Multiple shapes reconstruction ...“

$IMSMRA-LS$				
Step	$s=1$			
Object	1	2	3	$Average$
δ	8.4×10^{-2}	3.5×10^{-1}	3.2×10^{-2}	1.6×10^{-1}
Δ	1.8×10^{-2}	1.2×10^{-2}	8.2×10^{-2}	3.8×10^{-2}
Step	$s=2$			
Object	1	2	3	$Average$
δ	2.6×10^{-2}	4.3×10^{-2}	5.1×10^{-2}	4.0×10^{-2}
Δ	6.9×10^{-3}	3.9×10^{-3}	4.2×10^{-3}	5.0×10^{-3}
Step	$s=3$			
Object	1	2	3	$Average$
δ	2.8×10^{-3}	1.7×10^{-2}	4.5×10^{-2}	2.2×10^{-2}
Δ	1.3×10^{-3}	1.9×10^{-3}	4.3×10^{-3}	2.5×10^{-3}
$IMSA-LS$				
Step	$s=1$			
Object	1	2	3	$Average$
δ	4.2×10^{-3}	6.1×10^{-2}	4.5×10^{-2}	3.7×10^{-2}
Δ	1.8×10^{-2}	9.0×10^{-3}	1.0×10^{-2}	1.2×10^{-2}
$Bare-LS$				
Step	-			
Object	1	2	3	$Average$
δ	3.4×10^{-2}	$-$	3.2×10^{-2}	$-$
Δ	5.3×10^{-3}	4.0×10^{-2}	4.4×10^{-3}	1.6×10^{-2}

Table I - M. Benedetti *et al.* - “Multiple shapes reconstruction ...“

	$IMSMRA-LS$	$IMSA-LS$	$Bare-LS$
	$SNR = 20\,dB$		
$k_{opt}^{(1)}$	79	96	302
$\eta^{(1)}$	841	841	2500
$k_{opt}^{(2)}$	264	–	–
$\eta^{(2)}$	841	–	–
$k_{opt}^{(3)}$	53	–	–
$\eta^{(3)}$	805	–	–
f_{pos}	4.63×10^{11}	1.14×10^{11}	9.44×10^{12}

Table II - M. Benedetti *et al.* - "Multiple shapes reconstruction ..."

	$IMSMRA-LS$		$IMSA-LS$		$Bare-LS$	
ε	$<\delta>$	$<\Delta>$	$<\delta>$	$<\Delta>$	$<\delta>$	$<\Delta>$
2.5	2.3×10^{-2}	7.5×10^{-3}	4.4×10^{-2}	1.1×10^{-2}	1.6×10^{-1}	4.9×10^{-2}
3.0	3.2×10^{-1}	1.9×10^{-2}	2.8×10^{-1}	2.3×10^{-2}	3.4×10^{-1}	2.2×10^{-2}
4.0	6.8×10^{-1}	3.1×10^{-2}	6.8×10^{-1}	3.1×10^{-2}	8.2×10^{-1}	1.0×10^{-1}